Journal of Molecular Structure 1365 (2026) 145994

Contents lists available at ScienceDirect

Journal of Molecular Structure

journal homepage: www.elsevier.com/locate/molstr

# A simple synthesis and DFT approach of a new unsymmetrical dithizone as an efficient NLO substance: Thermal and experimental studies in a fluid medium

Amir Hussein Ali [a], Ahmed Majeed Jassem [b,*], H.A. Sultan [a], Qusay M.A. Hassan [a], C.A. Emshary [a], Wisam A. Radhi [c]

[a] *Department of Physics, College of Education for Pure Sciences, University of Basrah, Basrah 61001, Iraq*
[b] *Department of Chemistry, College of Education for Pure Sciences, University of Basrah, Basrah 61001, Iraq*
[c] *Department of Chemistry, Polymer Research Center, University of Basrah, Basrah 61001, Iraq*

ARTICLE INFO

*Keywords:*
Unsymmetrical dithizone
DFT
Thermal properties
NLO activity
Diffraction patterns

ABSTRACT

The objective of the present work is to synthesize a new unsymmetrical dithizone chromophore **8** namely, (*E*)-5-(4-nitrophenyl)-1-phenylthiocarbazone ($C_{13}H_{11}N_5O_2S$) using simple chemistry reactions. Upon identifying its chemical structure, the extensive computational, thermal, and experimental studies are devoted to investigate its nonlinear optical (NLO) activity. The theoretical outcomes disclosed that the target chromophore **8** showed high linear polarizability, $\alpha$ (esu), and first hyperpolarizability, $\beta$ (esu), owing to the ability of aromatic rings to extent electron density across $\pi$–conjugation in a direction towards the $NO_2$ substituent as a potent acceptor group. The molecular electrostatic potential (MEP) diagram, time-dependent density-functional theory (TD-DFT), Mulliken charges, and natural bond orbital (NBO) investigations are addressed theoretically. The thermal properties of the target chromophore **8** are studied through the assessment of its thermal conductivity (K), viscosity (η), and specific heat capacity ($c_p$) in addition to simulation of its thermal diffusion using a Finite difference method through solving the 2D transient heat conduction equation. By irradiating the target sample with continuous wave (CW) laser beams (473 and 532 nm), its NLO response is improved *via* the generation of diffraction patterns (DPs). The simulation results of DPs *via* the use of Fresnel–Kirchhoff integral are obtained with good accord compare to experimental results. For the target chromophore **8**, the properties related to its all-optical switching (AOS) are studied utilizing two CW visible laser beams. To have efficient materials for use in optoelectronic devices, the work findings strongly encourage to conduct this chromophore for further experimental investigations in order to reach this goal.

## 1. Introduction

Due to impactful and fascinating applications that featured by nonlinear optical (NLO) materials in the sophisticated electronic and optoelectronic systems, lot of interest has been paid to design or develop these materials with pronounced various applications [1,2]. Potential applications in terms of optoelectronic scope have spurred extensive investigations on new potential optical molecules involving exploitation of organic molecules [3,4]. By comparing with their inorganic counterparts, the structural alterations or modifications in the organic molecules can be achieved through feasible chemical synthesis with inexpensive cost for production [5,6]. In principles, essential factors offered by the organic materials make them as qualified materials for significant NLO properties [7]. Electronic delocalized conjugation, extending $\pi$-conjugated bridge, and induced dipole moment are some important factors that featured by organic NLO materials [8–10]. The enhancement of these factors in the potential NLO organic materials is significantly affected by an alteration in their molecular structures. These alterations might lead to improve their high NLO properties with short response times [11,12]. Logically, the presence of donor-$\pi$-acceptor system (D-$\pi$-A) and conjugated $\pi$-bridge nature in the organic candidate chromophores plays an important role in the NLO magnitudes involving polarizability ($\alpha$) and hyperpolarizability ($\beta$) [13,14]. Providing strong auxiliary $\pi$-electronic bridges in the D-$\pi$-A

---

* Corresponding author.
*E-mail address:* ahmed.majedd@uobasrah.edu.iq (A.M. Jassem).

https://doi.org/10.1016/j.molstruc.2026.145994
Received 12 January 2026; Received in revised form 2 March 2026; Accepted 14 March 2026

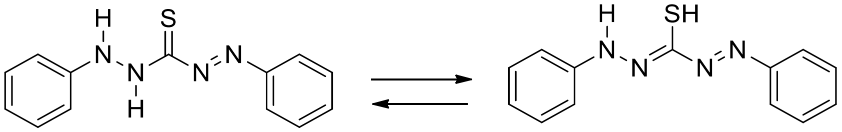

**Fig. 1.** Tautomeric configurations in a dithizone molecule.

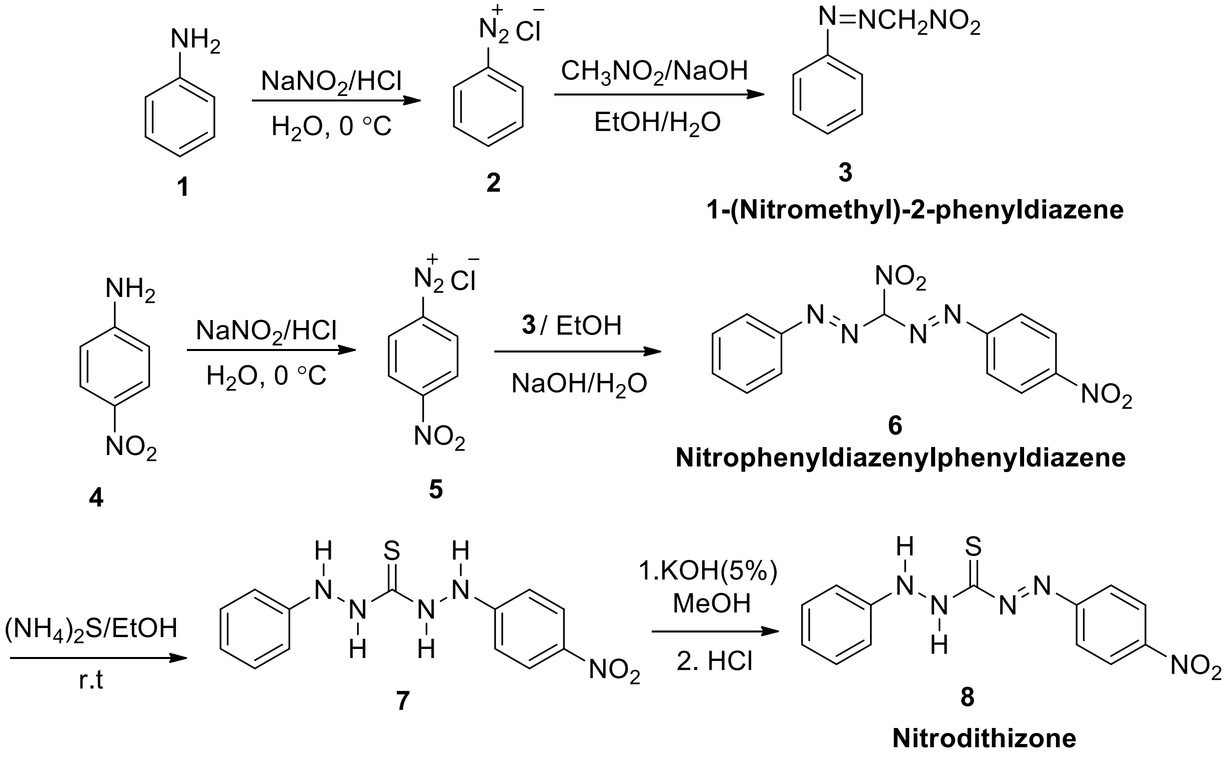

**Fig. 2.** Synthesis description of the new nitrodithizone derivative 8.

conjugation across the organic molecule backbone leads to form a push-pull configuration which acts to improve the molecular $\alpha$ and $\beta$ with larger NLO response and high thermal stability [15,16]. Based on recent studies, several organic materials have been designed and investigated for their NLO activities [17–19]. These studies declared in addition to the above mentioned factors that the chemical structures for organic molecules candidates should have crucial prerequisites in order to achieve potentially large NLO properties [20,21]. Among these requirements, the molecular arrangement in a non-centrosymmetric architecture possesses a strong electronic mobility, polarized positions (D and A substituents), and extensive charge transfer (CT) distribution in its D-π-A system [22–24]. In the latest researches on NLO organic materials, several accountable procedures have been established to promote the NLO activities, including extended π-electron conjugation, modification of central core bridges, and strengthening the tendency of donor/-acceptor parts in the molecule skeleton [25–27]. Beside the precedence above, extensive studies have thus been devoted to investigate organic materials, particularly non-centrosymmetric molecules as they are believed to hold promise for their potential photonic, nonlinear optic, and optoelectronic applications [28].

On the other hand, dithizone compounds are characterized from that the compounds contain a thiocarbazide chromophore. Dithizone derivatives are of interested classes of remarkable photochromic reactions as they are considered as an efficient candidate for diverse sensor applications [29,30]. Two different tautomeric configurations (thione and thiol forms, Fig. 1) are found in dithizone molecule [31] and this property is being conducted for improving its analytical applications for example, the synthesized GNPs modified with dithizone has been used as a Cu$^{2+}$ potentiometric sensing agent [32].

In other related published works, Taha *et al.* [33] synthesized multiferroic BFO nanoparticles modified with dithizone molecules as an immobilizing chromophore and investigated their optical sensing behavior towards some trace heavy metals. They demonstrated that the target synthesized nanoparticles act as a supreme optical sensor with highly sensitive and selective detection towards Cd $^{+2}$, Pb$^{+2,}$ Cr$^{+3}$, and Ni$^{+2}$. Furthermore, Alberti *et al* [34] have successfully prepared smart sensory substance based on dye dithizone molecule on a solid phase supported with triacetylcellulose membrane for photographic film. They proved that this prepared sensor with low cost can be efficiently used for determination of bivalent cations. Despite the sensory properties illustrated above, the dithizone derivatives might give potential applications that are not discovered yet particularly, in the photonic and optoelectronic fields.

Some methods have been introduced for synthesis of asymmetric and symmetric dithizone derivatives [35]. In the period 1882-1943, direct coupling of phenylhydrazine derivatives with carbon disulphide was the most common method as reported by Billman and Cleland [36]. The more recent method has been introduced to synthesize dithizone derivatives based on the coupling of diazo-derivatives in the presence of a reducing agent such as ammonia sulphide [37]. Considering the reported photochromic and potentiometric applications that offer by dithizone derivatives and their expected potential in the nonlinear optic, and optoelectronic fields, these compounds have highly garnered our attention.

We herein introduce an efficient procedure for synthesis of a new novel asymmetric dithizone containing alternate NO$_2$ group as a strong acceptor group. As shown in the synthesis chemistry (Fig. 2), many steps are adopted starting from phenyl diazonium chloride **2** which is prepared using a diazotization step of distilled aniline **1** with sodium nitrite ($NaNO_2$). An addition of nitromethane ($CH_3NO_2$) to the diazonium chloride **2** in the presence of an ethanolic NaOH solution would release intermediary 1-(nitromethyl)-2-phenyldiazene **3** as red precipitate. Under an ethanolic NaOH solution, the condensation step of the intermediate **3** with another prepared diazo derivative **5** of 4-nitro aniline **4** was completed to give the intermediary nitrophenyldiazenylphenyldiazene **6**. In the next step, the intermediate **6** is subsequently reduced through an excess addition of ammonium sulphide $(NH_4)_2S$ to afford a pure white thiocarbazide **7** as an unstable intermediate. The intermediate **7** is further oxidized in the presence of a methanolic KOH solution to give the orange K salt which is ultimately acidified with dilute solution of HCl to offer the target nitrodithizone derivative **8** as an orange-red precipitate. Various spectroscopic techniques and DFT computations were conducted to establish the structural verification of the target nitrodithizone **8**. As the prepared nitrodithizone **8** containing alternate $NO_2$ acceptor in its half electronic architecture, it should promote the push-pull system through the enhanced CT distribution. Thus, the improvement of thermal and NLO activities for the target nitrodithizone **8** is assessed using different measurements. The experimental evaluations of its thermal conductivity (K), viscosity (η), and specific heat capacity ($c_p$) in addition to its NLO response under adoption of continuous wave (CW) (473 and 532 nm as effective CW visible laser beams) for diffraction patterns (DPs) are the main goals for this work.

## 2. Experimental

Unless otherwise addressed, all chemicals and solvents were commercially obtained from common suppliers (Merck and Sigma-Aldrich) and utilized as received, without any further purifications. Reaction solutions utilizing doubly distilled water were accomplished using an ice cooling stirring container during synthesis. The progress and completion of the reactions to obtain the synthesized compounds with high purities, were checked using TLC plates (254-g/uv Merck). To detect and visualize the products spots, an eluent of ethyl acetate or acetone: hexane (1: 1) and an aqueous KMnO4 solution or UV light were used. A thermopan microscope apparatus was utilized to measure the melting points (m.p) of the solid products. NMR ($^1H$ and $^{13}C$) spectra at 298 K were recorded on a NEO-NMR spectrometer (Bruker Avance with frequencies operating at 400.0 for $^1H$ and 100.53 MHz for $^{13}C$). The signals patterns are presented according to chemical shift (*δ*) values of $Si(CH_3)_4$ and residual signals (DMSO-*d*$_6$) as the internal standard and nondeuterated solvent, respectively. IR spectra verifying the vibrational absorptions of essential functional bonds were recorded on a Shimadzu spectrophotometer (84005-FTIR) utilizing KBr disk for solid samples. A Shimadzu instrument (Agilent MSD/EI 70 eV/5 kHz) is utilized to document the mass data. UV–vis. measurement for the target nitrodithizone **8** was run in EtOH (200–700 nm) using a Shimadzu device (UV-2401PC) supplied with a non-separable glass cell (0.1 cm path) at room temperature (RT). For the target nitrodithizone **8**, three experimental set-ups are adopted to measure its thermal parameters viz., K, η, and $c_p$ where the first methodology is identified for *K* measurement [38], while the second and third ones are addressed elsewhere for η and $c_p$ measurements [39]. Upon the integrated calibration for a calorimeter was validated according to deionized water as a standard fluid, the $c_p$ performance of the target nitrodithizone **8** is obtained. The experimental set-ups for measuring η and $c_p$ values are found in the aforementioned reference [38]. The NLO activity of the target nitrodithizone **8** is evaluated using two wavelength laser beams 473 nm (power range of 0-66 mW) and 532 nm (power range 0-50 mW). Rayleigh range of the aforementioned beams are equal 2.456 and 2.763 mm. The two beams have spots with the same size of 1.5 mm (at $e^{-2}$). 19.235 μm as an effective spot size was set up for the first beam to be fitted with a glass lens (focal length of 5 cm), while the two beams were focused to spot sizes of 76.941 and 86.539 μm using two glass lens of foci 20 cm each. The beams powers were measured using multiple wavelength power meters. The liquid sample was put into a glass cell (1 mm). The falling ring patterns resulted on two semitransparent screen of 30 × 30 and 60 × 60 cm dimensions fixed at a position of 85 cm from exiting plane of the target sample cell. The two laser beams emitted from two solid state laser devices, each has CW character. One of the beams (λ = 473 nm) CW character changed to pulsed character using a frequency generator *via* the TTL function when needed. The DPs pictures were obtained using digital, 1/32 sec speed shutter camera. All experiments were further guided to follow experiment set ups given in reference [8] in order to study all-optical switching (AOS) of the target sample. Resulted DPs were studied via effect of beam wave front kind, effect of laser beam powers and the temporal DPs evolution.

### 2.1. *Synthesis of the target nitrodithizone derivative 8*

Nitrodithizone derivative **8** is synthesized according to an adopted method given in [40] under slight modifications as stated below:

#### 2.1.1. *Synthesis of 1-(nitromethyl)-2-phenyldiazene 3*

In a 100 mL beaker supplied with ice path, freshly distilled aniline (18 g, 0.2 mol) was treated with con. HCl (0.1 mol, 25 mL) and doubly distilled water (40 mL) under a cooling stirrer (0 °C). To above content, 30 mL of an aqueous solution containing $NaNO_2$ (17 g, 0.2 mol) was slowly dropped under vigorously cooling stirrer (30 min) till a clear solution is formed. The resulting diazo solution **2** was cooled and slowly added to an alkaline mixture of NaOH (8 g, 0.2 mol), $CH_3NO_2$ (12 g, 0.2 mol), EtOH (75 mL), and $H_2O$ (25 mL). The high concentration alkaline NaOH was used to deprotonate $CH_3NO_2$ molecules and to neutral any residual HCl formed as a side product. The resulting mixture was additionally stirred for 30 min and further treated with distilled water (200 mL). The purification of the target product was carried out by trituration with cold water. A large Buchner funnel was conducted to collect the yellow-orange precipitate to give 1-(nitromethyl)-2-phenyldiazene **3**, yield (70%), m.p. 85-86 °C.

#### 2.1.2. *Synthesis of nitrophenyldiazenylphenyldiazene 6*

To a beaker reaction (50 mL), a cooled solution of conc. HCl (0.1 mol, 10 mL) and distilled water (20 mL), 4-nitro aniline **4** (7 g, 0.05 mol) was added at 0 °C. To above mixture, an aqueous solution (10 mL) of $NaNO_2$ (5 g, 0.05 mol) was slowly dropped under vigorously cooling stirrer (30 min) till a clear yellow solution is formed. The resulting diazo solution **5** was added dropwise to a stirring solution of the prepared 1-(nitromethyl)-2-phenyldiazene **3** (8 g, 0.05 mol), EtOH (25 mL), NaOH (8 g, 0.2 mol), and $H_2O$ (10 ml) at 0 °C. Upon the above mixture was stirred for 20 min, the mixture was treated with cold water (200 mL) and adjusted to pH = 7 using an alkaline solution of NaOH (2M). The separated brick-red precipitate was collected through a Buchner funnel filtration and dried under warm oven. To a conical flask (100 mL) charging with dry $CH_2Cl_2$ (50 mL), the separated brick-red precipitate was added and heated at 35-40 °C for 10 min. The product was ultimately collected after cooling step, and it was further purified through trituration with cold $CH_2Cl_2$ and filtrated to afford the entitled intermediate **6**, yield (60%), m.p. 166-168 °C.

#### 2.1.3. *Synthesis of nitrodithizone derivative 8*

To a lightly stoppered conical flask containing absolute EtOH (60 mL), the prepared nitrophenyldiazenylphenyldiazene **6** (3.14 g, 0.01 mol) was added. The suspended solution was further placed in an ice bath (0-3 °C) and stirred for 20 min. While stirring, the above content was saturated with as an ethanolic solution of ammonium sulphide (20%, 10 mL). After the end of reaction as indicated by the disappearance of orange-brown color solution, the white sediment product is precipitated. To above content, crushed ice of distilled water (50 mL)

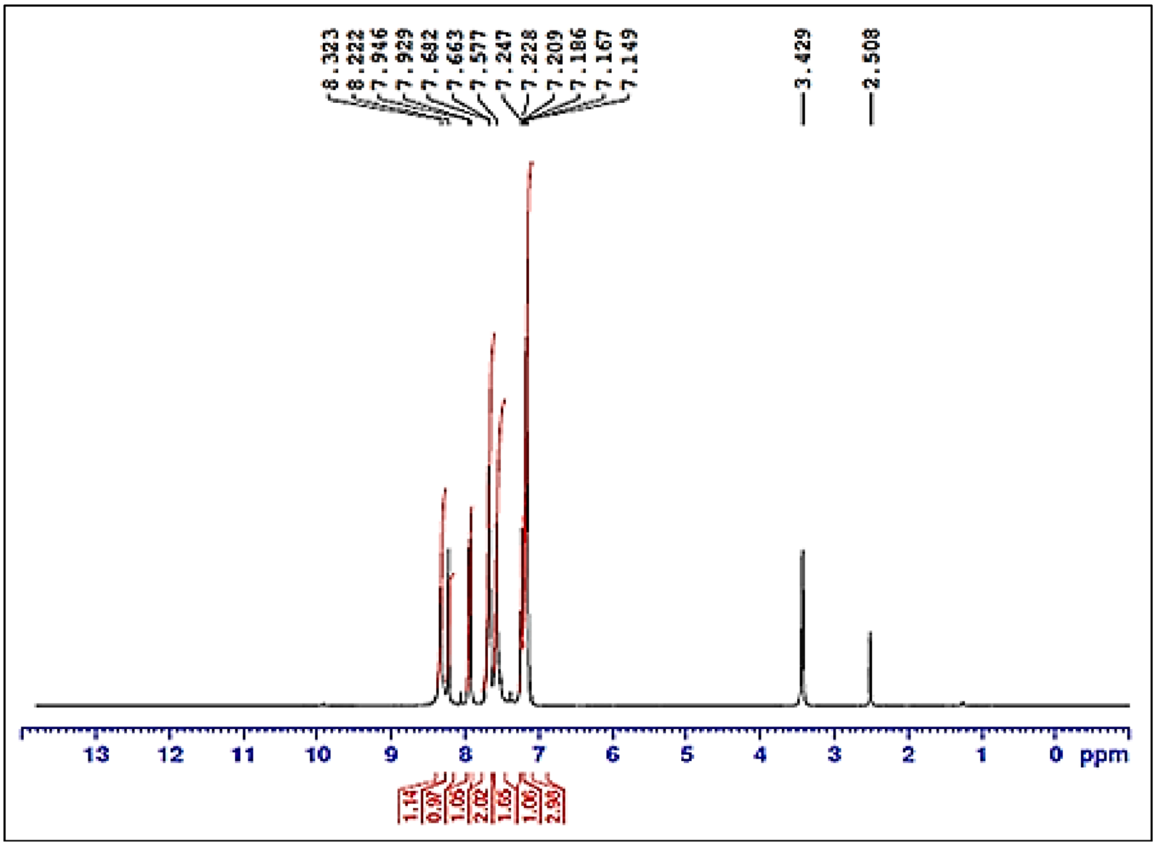

**Fig. 3.** $^1$HNMR chart of nitrodithizone derivative 8.

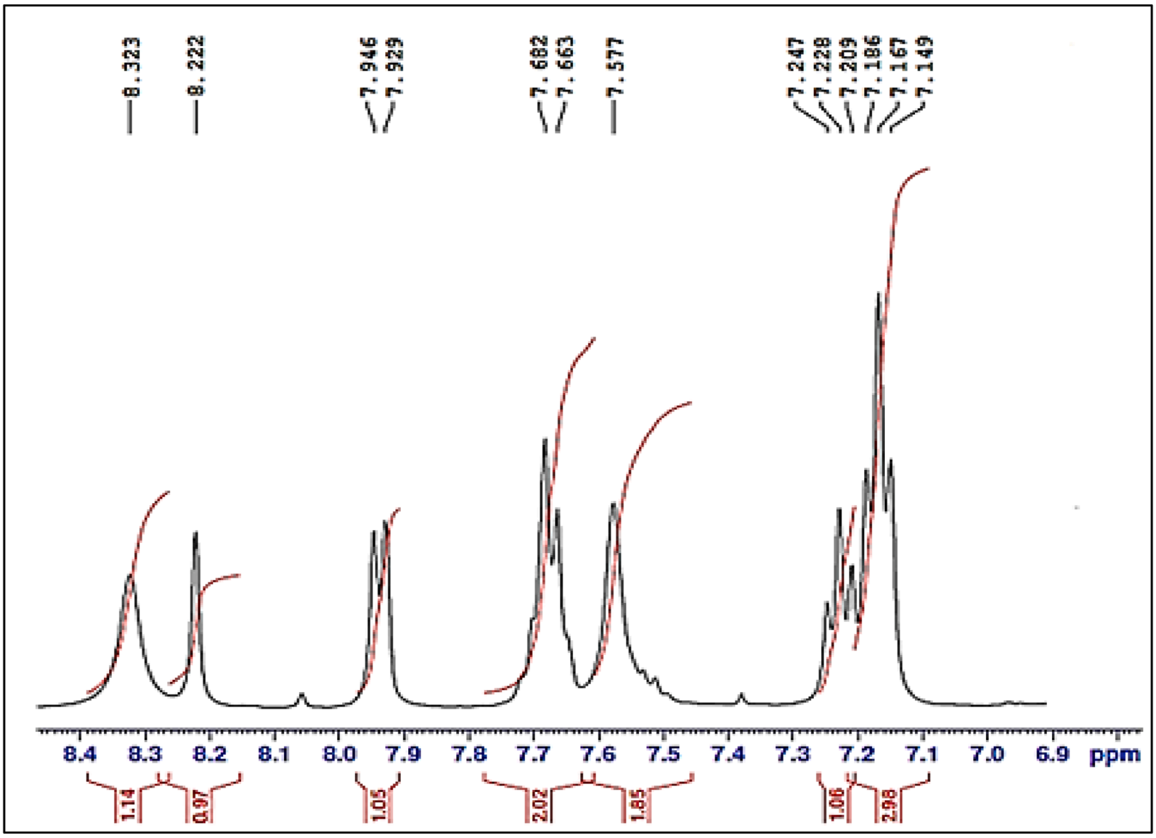

**Fig. 4.** $^1$HNMR expansion chart of nitrodithizone derivative **8** found in Fig. 3.

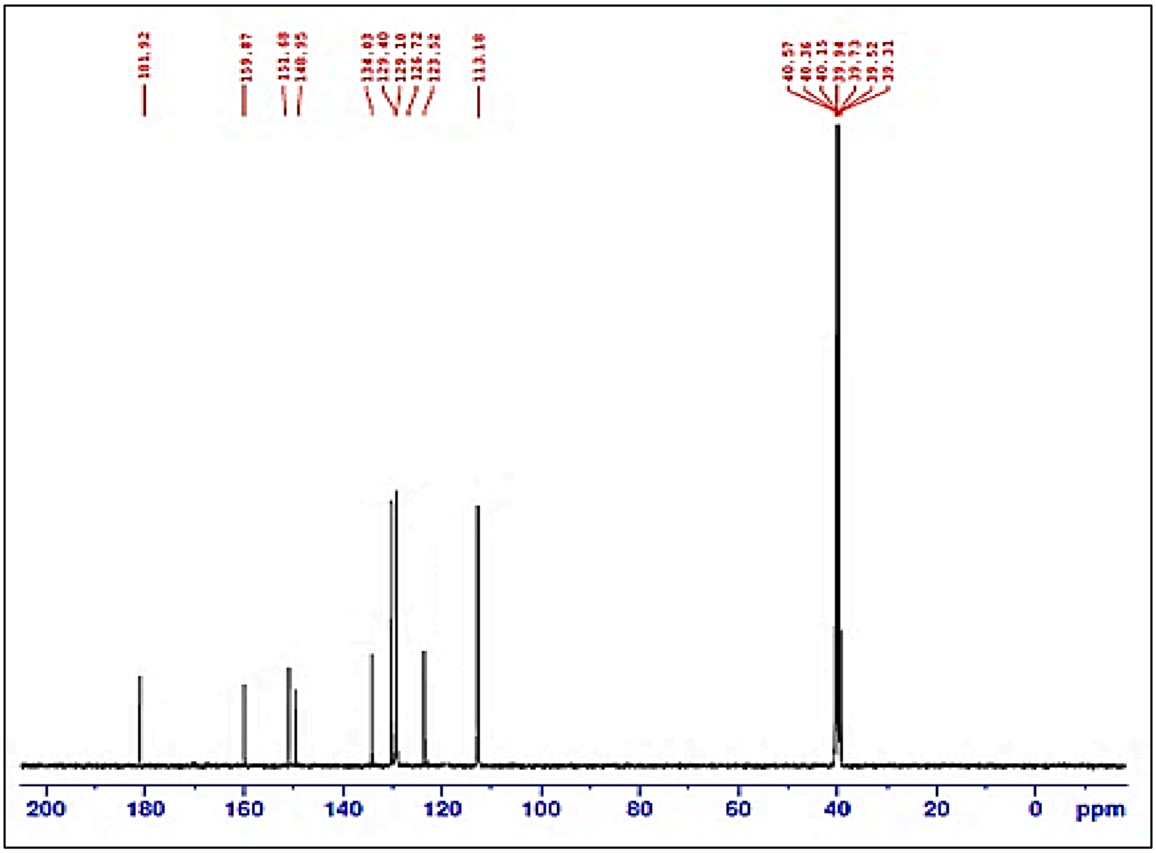

**Fig. 5.** $^{13}$CNMR chart of nitrodithizone derivative 8.

was poured to raise precipitation. The precipitate was immediately filtered off, collected, and thoroughly washed with distilled water to give the pure white thiocarbazide **7**. After the intermediate thiocarbazide **7** was dried, it was oxidized with a methanolic KOH solution (5%, 60 mL) to give orange-red K salt solution. Upon the salted solution was filtered off, it was acidified with a few dropwise of con. HCl till pH= 2. The orange-red precipitate was gravity filtered and several times washed with distilled water. The purification of final product **8** was completed using a crystallization step from methanol and subsequently dried to afford the pure nitrodithizone derivative **8**, yield (55%), m.p. 172-173 °C.

### 2.2. *Spectroscopic characterizations of the target nitrodithizone derivative 8*

The structural elucidation of the unsymmetrical dithizone derivative **8** was established by its spectral data including NMR, FT-IR, and Mass spectroscopies. The protons resonances of aromatic systems in $^1$HNMR spectrum (Figs. 3 and 4) appeared based on their integrations. In the range of chemical shifts ($\delta$ 8.32–7.14 ppm), the residual protons for two benzene rings are found to possess the data as follows: 7.17 (3H, t, $J =$ 3.4 Hz), 7.23 (1H, t, $J =$ 2.6 Hz), 7.68-7.57 (4H, m), and 7.93 (1H, d, $J =$ 2.7 Hz). As mentioned earlier, the dithizone molecule found in two tautomers (thione and thiol), the signals of thiol proton and two NH protons are notably absent, indicating the creation of the nitrodithizone derivative **8** in a thione form. Indeed, two clear signals of protons came into view in $^1$H NMR due to the presence of two NH groups at $\delta$ 8.22 and 8.32 ppm. In the $^{13}$CNMR spectrum (Fig. 5), the distinguished signal for carbon (C=S) is found at the low field (181.9 ppm), indicating the thione tatumor found in nitrodithizone derivative **8**. The other corresponding signals appeared at 159.8 and 151.7 ppm are due to the quarter aromatic carbons that attached with thiocarbazone moiety. The carbon signal positioned at 148.9 ppm is due to quaternary carbon that carries $NO_2$ group. Furthermore, the other signals located at the high field 134.0, 129.4, 129.1, 126.7, 123.5, and 113.2 ppm are corresponding to Ar-CH systems. The distinctive residues for aromatic carbons in the nitrodithizone derivative **8** are good consistency with the drawn structure. Different bands related to stretching vibrations in FT-IR (Fig. 6) appeared corresponding to the following functional groups: two N–H groups at 3441 and 3278 cm$^{-1}$ and aromatic C–H stretching bands at 3053 cm$^{-1}$. In the region 1591–1496 cm$^{-1}$, sharp bands are noted due to aromatic C=C bonds. Furthermore, a distinctive band was detected at 1215 cm$^{-1}$ is related to the stretching vibration in C=S bond. The drawn structure of nitrodithizone derivative **8** verified its mass spectrum (Fig. 7). In this spectrum, an intensive mass peak with abundance intensity (80000) is highlighted at $m/z = 301.2$ pertaining to the accuracy of the molecular weight: $[M]^+$, $C_{13}H_{11}N_5O_2S^+$. In addition, the other characteristic peaks at varied regions corresponded to fragments which are in in relative correspondence with the correct structure.

### 2.3. *UV-visible study*

Significant insights into the nature of transitions and charge transfer absorption for organic compounds can be verified by the practical UV-visible spectrum. In Fig. 8, the experimental UV-visible spectrum displays the absorbance peaks of electronic transitions occurred in the nitrodithizone derivative **8** ($1 \times 10^{-4}$ M in EtOH) with a range of 300-700 nm. In around visible absorption, two distinctive peaks are observed at wavelengths of $\lambda_{max}$ 468 and 604 nm. The peak that takes place at the shorter wavelength ($\lambda_{max}$ 468 nm) is predicted due to $n \rightarrow \pi^*$ transition that is formed from the presence of C=S and $NO_2$ chromophores. The other strong peak with longer wavelength ($\lambda_{max}$ 604 nm, bathochromical shift) can be ascribed to $\pi \rightarrow \pi^*$ transition that occurs in aromatic groups. Under unique consideration regarding calculating the linear absorption coefficients ($\alpha$) using an equation [41], the $\alpha$ values of

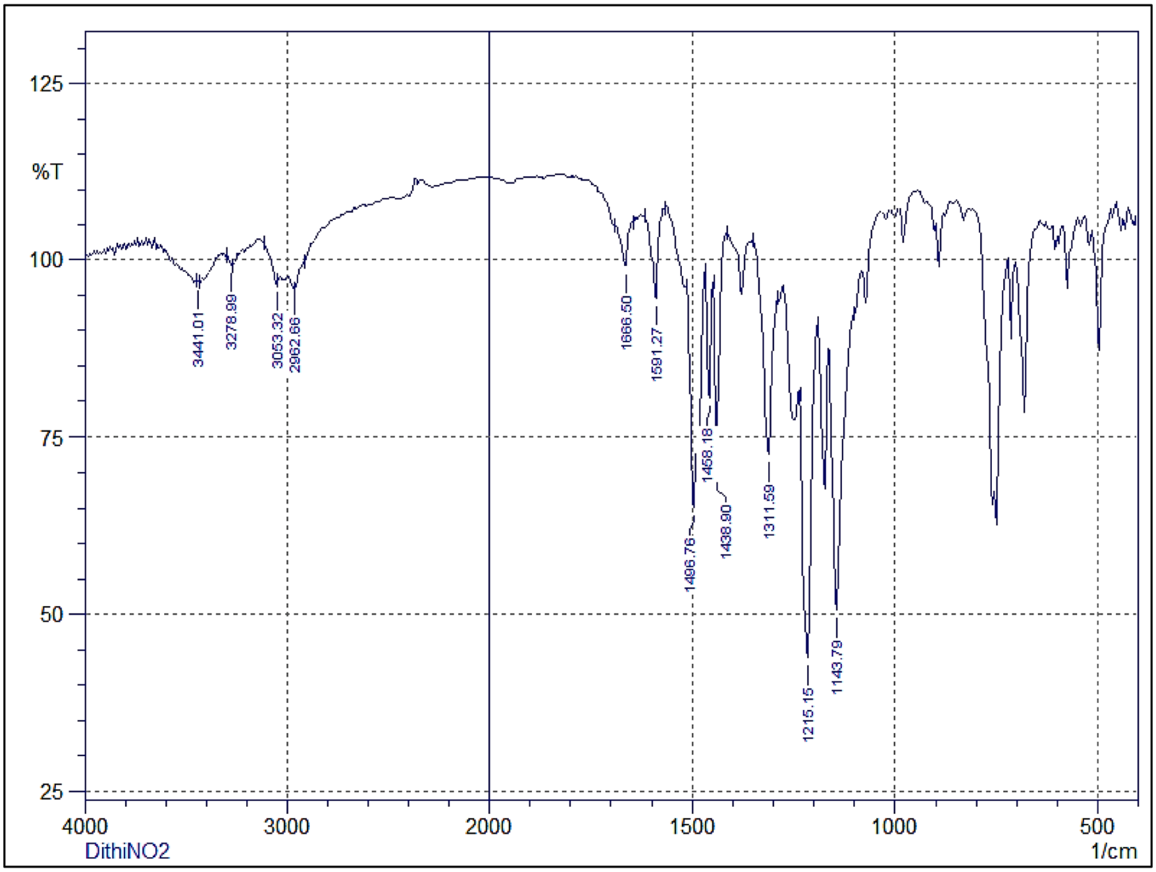

**Fig. 6.** FT-IR chart of nitrodithizone derivative 8.

the recorded absorptions in the target nitrodithizone **8** were found to equal $\alpha_{473}$=7.64 and $\alpha_{532}$ =4.33 cm$^{-1}$ in correspondence with the slandered wavelengths at 473 and 532 nm, respectively.

## 2.4. DFT analysis

DFT calculations for the target derivative **8** were performed utilizing the database Gaussian 09 package and analyzed under Gauss software (view 5.0.43) [42,43]. The theoretical calculations were conducted to full optimization of the geometric target derivative **8** using B3LYP functional complemented with the 6-311G (d,p) basis set [44,45]. In the absence of any symmetry restrictions, the geometric structure (Fig. 9a) of the target derivative **8** at its minimum total energy was successfully completed by testing its negative vibrational frequencies. The molecular electrostatic potential (MEP) for the target derivative **8** was also simulated using the aforementioned functional at the same basis level. The computed MEP map offers a powerful visual details in terms of surface, charge distributions, potential electrostatic interactions (positive electrophilic and negative nucleophilic regions), intermolecular interactions, electronegativity, and enhancing the visible polarization of electronic sites that would release onto electron density surface [46,47]. 3D topographical electrostatic surface of MEP as given in Fig. 9b shows different intense reactive sites as depict by different colors. According to aforementioned figure, the bright red regions (electron-rich) mainly localized around the S, O and N atoms with a negative electrostatic charge, whereas the blue regions (electron-deficient) concentrated around the hydrogen atoms refers to the positive electrostatic charge. Furthermore, the yellowish and bright green regions indicate the existence of the slight electronic rich (π-phenyl rings) and zero potential regions, respectively. Obviously, the calculated electron densities values on the S, O and N atoms (the deep negative sites) were acquired as -2.897, -2.643, and -3.803 au, respectively, whereas the value for the H atom as a high positive site is 6.258 au.

All other parameters that have great influence on electronic and NLO characteristics were thoroughly executed at the above-mentioned level. These parameters are focused on global reactivity inspection of the orbitals energy difference in order to determine the quantum descriptors such as the energy band gap ($E_{HOMO}$–$E_{LUMO}$), ionization potential, I (eV), electron affinity, A (eV), electrophilicity index, $\omega$ (eV), hardness, η (eV), chemical softness, S (eV) $^{-1}$, electronegativity, $\chi$ (eV), and chemical potential μ (eV). The narrowest value of the energy band gap (1.6996 eV) is obtained from energy values of −5.3764 and −3.677 eV for HOMO and LUMO, respectively. This case indicates a characteristic intra-molecular CT (powerful push–pull effect) which takes place throughout the target chromophore **8**. The descriptors related to its electronic structure are obtained from energy value of $E_{HOMO}$–$E_{LUMO}$ (Fig. 10). The calculated values in terms of I (eV), A (eV), $\omega$ (eV), η (eV), S (eV) $^{-1}$, $\chi$ (eV), and μ (eV) are found to equal 5.376 (eV), 3.6768 (eV), 12.056 (eV), 0.8498 (eV), -0.425 (eV)$^{-1}$, 4.5266 (eV), -4.527 (eV), respectively. In addition, the important values of linear polarizability, $\alpha$ (esu), and first hyperpolarizability, $\beta$ (esu), were also computed as they serve as crucial descriptors to characterize NLO properties. The target nitrodithizone **8** showed highest nonlinear behavior as the calculated maximum values of $\alpha$ and $\beta$ were 23.243 × 10$^{-22}$ and 412.605 × 10$^{-28}$ esu, respectively. In the non-linear optic field, the assessment of optical parameters such as hyperpolarizability, $\beta$ (esu) is important for efficient NLO response. The $\beta$ value of the target nitrodithizone **8** was computed and thereby its efficiency compared with structurally related dithizone-based NLO materials reported in the previous works, is introduced. For examples, the synthesized (*E*)-2-ethylidenehydrazinecarbothioamide exhibited a $\beta$ value of 252.77 × 10$^{-33}$ esu [48], while the designed (*E*)-2-(1-phenylethylidene)hydrazinecarbothioamide performed a

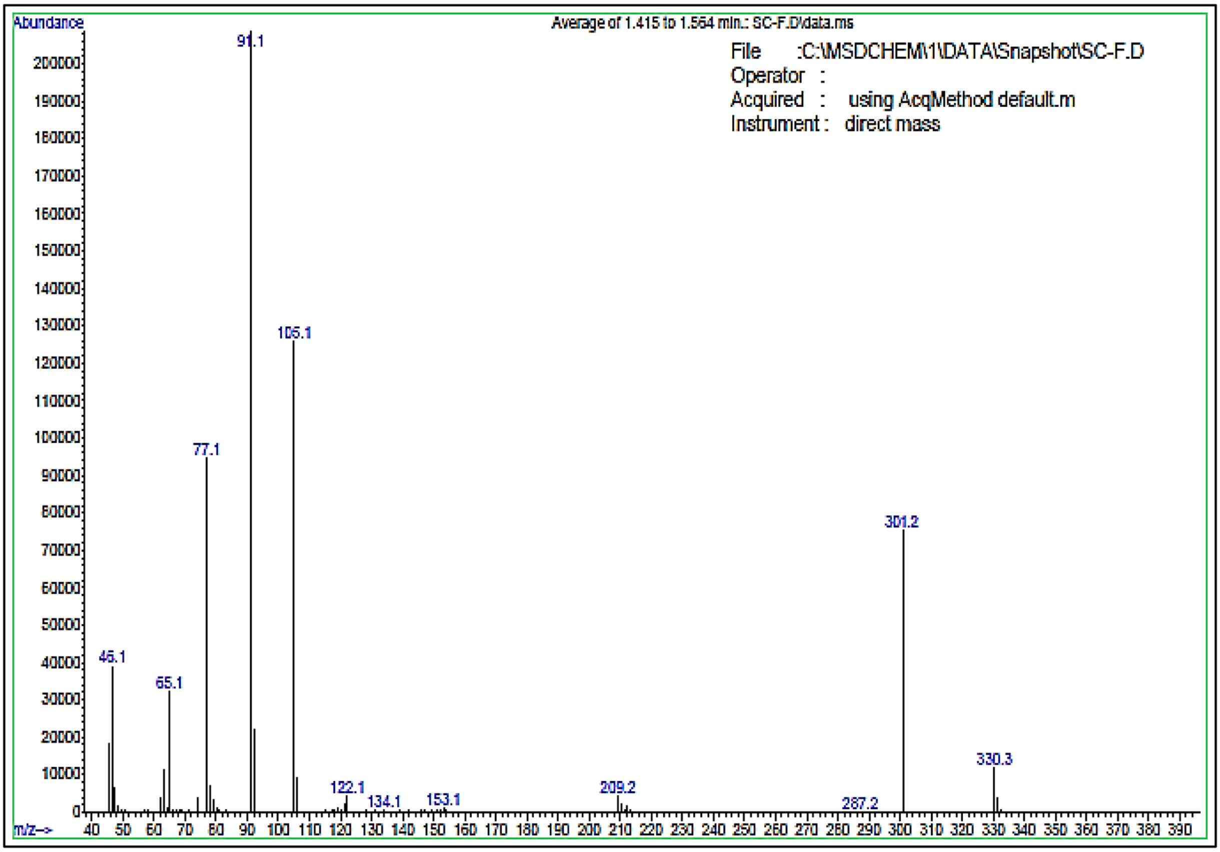

**Fig. 7.** EI-Mass chart of nitrodithizone derivative 8.

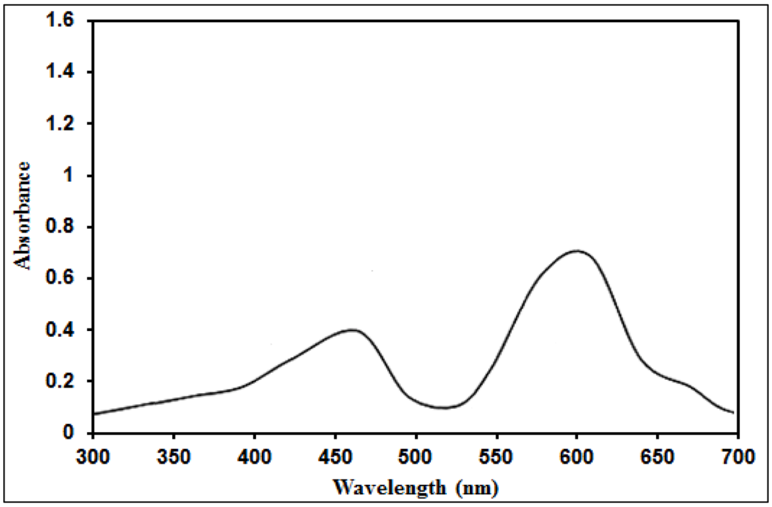

**Fig. 8.** Experimental UV-visible chart of the nitrodithizone derivative 8.

remarkable $\beta$ value of 5.181 × $10^{-30}$ esu [49]. Furthermore, a very close structurally related structure of the nitrodithizone derivative **8** was synthesized with absence of N-H in its architecture, namely (*E*)-*N*-(2-chlorobenzyl)-2-(2-hydroxybenzylidene)hydrazinecarbothioamide and its $\beta$ value found to have 4.812 × $10^{-30}$ esu [50]. Comparison with the aforementioned compounds demonstrates that the target nitrodithizone 8 exhibited efficient $\beta$ value (412.605 × $10^{-28}$ esu) since such value is times greater than *para*-nitroaniline (p-NA, 3.610 × $10^{-31}$ esu) reported as a prototype NLO material [51]. This probably due to the presence of a decrease in band gap and excitation energy as well as the enhancement above values typically rely on the $\pi$-conjugation delocalization within the entire molecule which can be extended by alteration of the potent substituents (donor and acceptor groups) attached to the molecule skeleton. The optical parameters obtained for the target derivative **8** make it as a promising NLO material.

TD-DFT computations were performed to acquire the theoretical spectrum of UV-visible for the nitrodithizone **8**. The calculated data in terms of transition levels, coefficients, lowest energies of excitation levels (eV), wavelengths (nm), and oscillator strengths (f) are listed in Table 1. The spectrum simulated from aforementioned B3LYP functional with basis sets of 6-311G (d,p) is depicted in Fig. 11. The calculations showed some electronic transitions that occur from the HOMO to LUMO

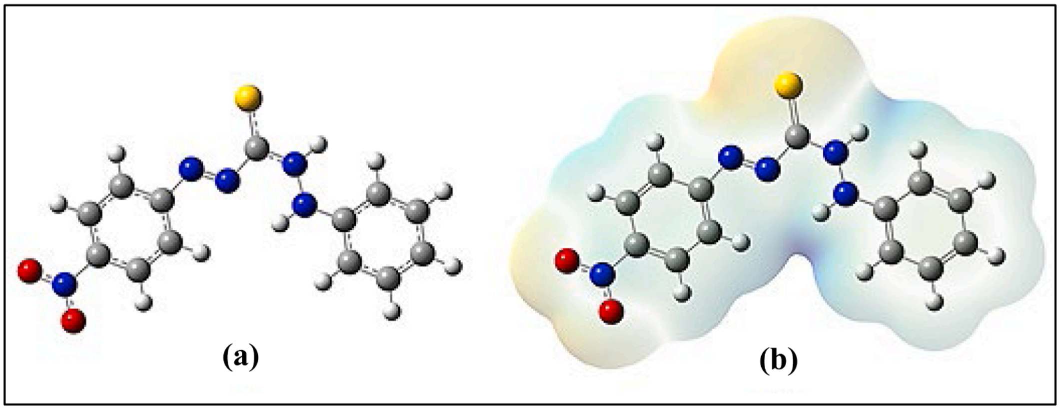

**Fig. 9.** (a) Optimal geometry and (b) 3D-MEP map of nitrodithizone derivative 8.

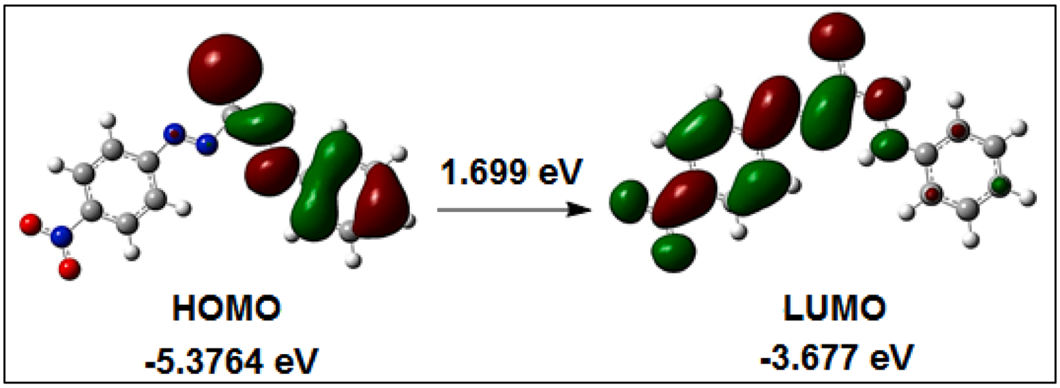

**Fig. 10.** Topographical representation (HOMO=-LUMO) in the nitrodithizone derivative 8.

**Table 1**
Theoretical data of UV-vis. spectrum computed by TD-DFT/B3LYP/6-311G (d,p) for the target nitrodithizone 8.

| State | Assignment | Coefficient | Energy (eV) | Wavelength (nm) | Oscillator Strength (f) |
|---|---|---|---|---|---|
| $S_0 \rightarrow S_1$ | HOMO-6 → LUMO<br>HOMO-5 → LUMO<br>HOMO-5 → LUMO+2<br>HOMO → LUMO+2 | 66%<br>12%<br>11%<br>14% | 3.8042 | 325.91 | 0.0198 |
| $S_0 \rightarrow S_2$ | HOMO-6 → LUMO<br>HOMO → LUMO+3 | 13%<br>69% | 3.7147 | 333.77 | 0.0095 |
| $S_0 \rightarrow S_4$ | HOMO-4 → LUMO | 70% | 3.1889 | 388.80 | 0.0037 |
| $S_0 \rightarrow S_6$ | HOMO-2 → LUMO | 69% | 2.7315 | 453.90 | 0.1951 |
| $S_0 \rightarrow S_7$ | HOMO → LUMO+1 | 70% | 2.6843 | 461.88 | 0.0469 |

levels. The state of $S_0 \rightarrow S_1$ due to n-π* consisted four electronic transition bands at 325.91 nm with energy of 3.8042 eV and 0.0198 oscillator strength f. For this transition, the orbital contributions are 66%, 12%, 11%, and 14% from HOMO-6 to LUMO, HOMO-5 to LUMO, HOMO-5 to LUMO+2, and HOMO to LUMO+2, respectively. At 333.77 nm, two bands for $S_0 \rightarrow S_2$ appeared with 3.7147 eV and 0.0095 oscillator strength f due to the orbital contributions from HOMO-6 to LUMO and HOMO to LUMO+3. The other two bands at 388.80 and 453.90 nm stated for $S_0 \rightarrow S_4$ and $S_0 \rightarrow S_6$, respectively, are assigned to π-π* transition. These bands are potentially based on the transitions occurred from HOMO-4 to LUMO (3.1889 eV) and HOMO-2 to LUMO (2.7315 eV) with contribution percentages of 70% and 69%, respectively. In the simulated spectrum, a band emerging from the main $S_0 \rightarrow S_7$ state occurred at 461.88 nm (2.6843 eV) is assigned to n-π* transition. This transition originated from HOMO to LUMO+1 with transition coefficients of 70%. This band is mainly very close to an intense peak ($\lambda_{max}$ 468 nm) appeared in the experimental spectrum for the target nitrodithizone **8** (Fig. 8). This dominant peak is assigned to the main transitions occurred from HOMO to LUMO, since these orbitals included are of n and π types. The results combined from practical measurement and theoretical calculations demonstrated high coincide with regards to their mean transitions. In summary, the active ICT interactions could be a result of charge transfer from the NH, C=S, and aromatic moieties as an electron donor to $NO_2$ group as an electron acceptor. This acts to enhance the dipole property to be intensified along molecule and increase polarity across its longitudinal axis.

The distribution of Mulliken charges is presented in Table 2 and its diagram is depicted in Fig. 12a and b. Based on the distribution level, the negative charges mainly positioned on the nitrogen, oxygen, and sulfur atoms. The charges exhibited with values of -0.47437, -0.38987, -0.38701, and -0.32675 are corresponding to N7, O21, O20, and N8, respectively. These atoms have the same color and more negative than other atoms in the synthesized nitrodithizone **8**. The less negative charges redistributed in other atoms involving N11, N12, and S10 (C=S bond) with values of -0.28402, -0.23746, and -0.23424, respectively. While, the charges that distributed in the carbon atoms (C1, C2, C4, C5, C6, C14, C15, C17, and C18) of aromatic rings were faded negative. According to distribution diagram, N19 atom of $NO_2$ group was more

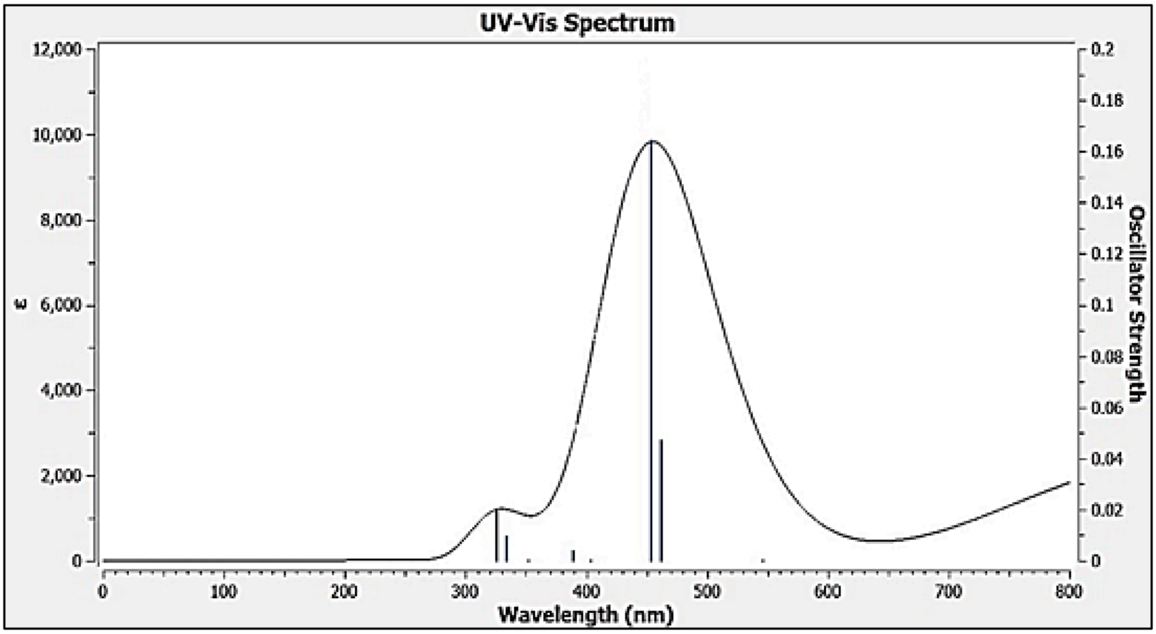

**Fig. 11.** The theoretical spectrum of the target nitrodithizone **8** simulated by TD-DFT.

**Table 2**
Mulliken population data and NBO analysis for the synthesized nitrodithizone 8.

| Mulliken analysis | | NBO analysis | | | | | |
|---|---|---|---|---|---|---|---|
| Atoms | Charges | Donor(*i*) | Occupancy ED/e | Acceptor(*j*) | E(*j*)-E(*i*) a.u. | F(*i, j*) a.u. | E$^{(2)}$ Kcal/mol |
| C1 | -0.09135 | σ (C1-C2) | 1.97728 | σ*(C3-N7) | 1.14 | 0.065 | 4.65 |
| C2 | -0.12941 | π (C1-C2) | 1.70709 | π* (C3-C4) | 0.27 | 0.073 | 22.75 |
| C3 | 0.38358 | π (C3-C4) | 1.63087 | π*(C5-C6) | 0.29 | 0.074 | 23.2 |
| C4 | -0.12968 | π (C5-C6) | 1.65433 | π*(C1-C2) | 0.27 | 0.074 | 24.76 |
| C5 | -0.08822 | π (C9-S10) | 1.96114 | π*(C9-S10) | 0.21 | 0.030 | 4.18 |
| C6 | -0.09111 | π (C9-S10) | 1.96114 | π*(N11-N12) | 0.23 | 0.036 | 6.35 |
| N7 | -0.47437 | π (N11-N12) | 1.90102 | π*(C9-S10) | 0.33 | 0.068 | 14.02 |
| N8 | -0.32675 | π (N11-N12) | 1.90102 | π*(C13-C14) | 0.40 | 0.060 | 9.95 |
| C9 | 0.342868 | π (C13-C14 | 1.58532 | π*(N11-N12) | 0.23 | 0.067 | 21.35 |
| S10 | -0.23424 | π (C13-C14) | 1.58532 | π*(C15-C16) | 0.27 | 0.069 | 21.08 |
| N11 | -0.28402 | π (C15-C16) | 1.63697 | π*(N19-O20) | 0.15 | 0.057 | 23.04 |
| N12 | -0.23746 | π (C17-C18) | 1.66039 | π*(C15-C16) | 0.28 | 0.068 | 20.41 |
| C13 | 0.24998 | π (N19-O20) | 1.98488 | LP3O21 | 0.18 | 0.078 | 12.45 |
| C14 | -0.08734 | LP(1)N7 | 1.72668 | π*(C3-C4) | 0.30 | 0.097 | 36.18 |
| C15 | -0.09532 | LP(1)N8 | 1.59310 | π*(C9-S10) | 0.22 | 0.117 | 71.77 |
| C16 | 0.256118 | LP(1)S10 | 1.98643 | σ*(C9-N11) | 1.04 | 0.056 | 3.61 |
| C17 | -0.10524 | LP(2)S10 | 1.86155 | σ*(N8-C9) | 0.64 | 0.075 | 10.67 |
| C18 | -0.06129 | LP(2)S10 | 1.86155 | σ*(C9-N11) | 0.54 | 0.079 | 14.12 |
| N19 | 0.391085 | LP(1)N11 | 1.94022 | σ*(C9-S10) | 0.74 | 0.073 | 8.88 |
| O20 | -0.38701 | LP(1)N12 | 1.95392 | σ*(C13-C18) | 0.95 | 0.081 | 8.63 |
| O21 | -0.38987 | LP(1)O20 | 1.98107 | σ*(C16-N19) | 1.07 | 0.062 | 4.26 |
| H22 | 0.095343 | LP(2)O20 | 1.89653 | σ*(C16-N19) | 0.56 | 0.076 | 13.03 |
| H23 | 0.08046 | LP(2)O20 | 1.89653 | σ*(N19-O21) | 0.71 | 0.105 | 19.29 |
| H24 | 0.080399 | LP(2)O21 | 1.89711 | σ*C16-N19) | 0.56 | 0.076 | 12.93 |
| H25 | 0.093562 | LP(2)O21 | 1.89711 | σ*(N19-O20) | 0.71 | 0.105 | 19.20 |
| H26 | 0.088783 | LP(3)O21 | 1.43916 | π*(N19-O20) | 0.14 | 0.139 | 164.47 |

positive due to this atom attached directly with tow electronegative oxygen atoms. Furthermore, the carbon atoms C3, C9 (C=S), C13, and C16 were found to be positive with an uneven distribution compared with compared with adjacent carbon atoms. In addition, the hydrogen atoms attached even to nitrogen or carbon atoms displayed positive charges with a range of value (0.080399 to 0.310638). The Mulliken population found in the nitrodithizone **8** highlighted the resultant dipole moment direction (4.6732 Debye), demonstrating the electronic activity and optical polarizability that are subtilized the NLO efficiency.

Natural bond orbital (NBO) analysis is significantly accomplished to gain clear insights into interpretation of charges transfer, inter-and intramolecular transitions, interactions between bonds, and hyperconjugative interactions [52,53]. NBO probe also grants a good indication about the hydrogen bonding and relocation of internal charges in D−π−A systems [54]. Herein, NBO computations were performed for the optimized nitrodithizone **8** using B3LYP/6-311G (d,p) method in order to elucidate the electronic delocalization occurred in bonding and anti-bonding orbitals inside the target molecule. The calculated outcomes of NBO transitions for the target nitrodithizone **8** are tabulated in Table 2. This Table shows NBO descriptors in terms of orbital types (donor (*i*) and acceptor (*j*)), electronic occupancy (ED/e), difference energies between acceptor and donor orbitals (E(*j*)-E(*i*)), NBO Fock

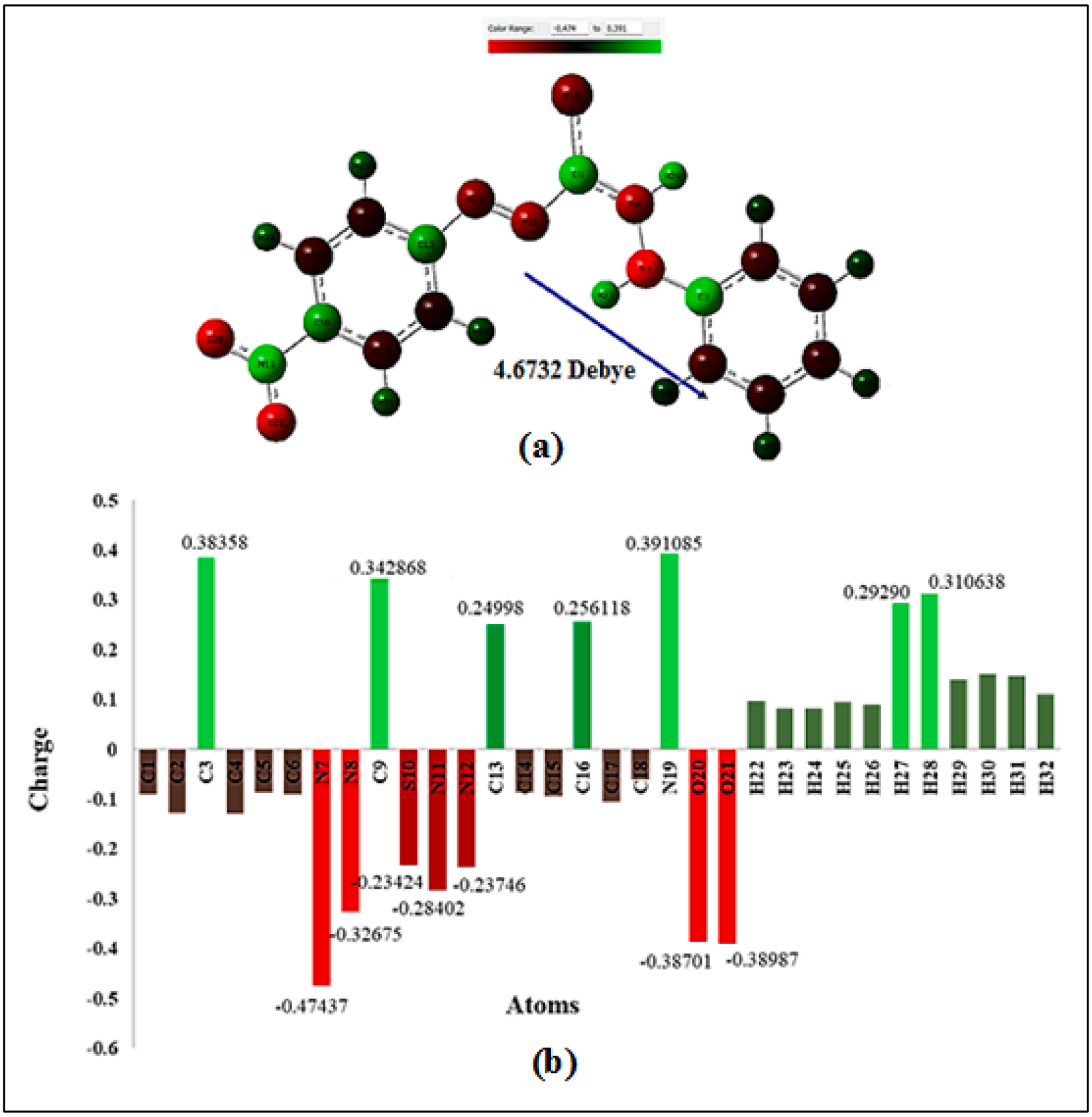

**Fig. 12.** (a) Charge distribution with dipole moment and (b) Mulliken population in the synthesized nitrodithizone 8.

matrix factor F(*i, j*) and second-order perturbation energy ($E^{(2)}$) which depicts the stabilization energy related to the measurement of intra-molecular interactions of D–A [55]. The main NBO transitions detected were σ → σ*, π → π*, LP → π*, and LP → σ* for the dithizone chromophore **8**. In σ → σ* type, one transition of σ(C1-C2)→σ*(C3-N7) presented smallest stability with a $E^{(2)}$ value of 4.65 Kcal/mol. Other types of significant transitions π → π* (D-A, ICT) such as π(C1-C2) → π*(C3-C4), π(C3-C4)→π*(C5-C6), π(C5-C6)→π*(C1-C2), π (C9-S10)→π*(C9-S10), π(C9-S10)→π*(N11-N12), π (N11-N12)→π*(C9-S10), π (N11-N12)→π*(C13-C14), π (C13-C14)→ π*(N11-N12), π(C13-C14)→π*(C15-C16), π(C15-C16)→π*(N19-O20), and π(C17-C18)→π*(C15-C16) are noticed with $E^{(2)}$ values of 22.75, 23.2, 24.76, 4.18, 6.35, 14.02, 9.95, 21.35, 21.08, 23.04, and 20.41 Kcal/mol, respectively. The one electron transition between the bonding orbital π (N19-O20) and lone pair LP3O21 was found with a small $E^{(2)}$ value of 12.45 Kcal/mol. The favorable electronic transitions found in the donor-to-acceptor trajectory are corresponding to intermediate types of LP→π* and LP→σ*. The unpaired electrons of LP→π* transitions are most prominent interactions having higher values of $E^{(2)}$. Among them, LP(1)N7→π*(C3-C4), LP(1)N8→π*(C9-S10), and LP(3)O21→π*(N19-O20) exhibited higher values of $E^{(2)}$ of 36.18, 71.77, and 164.47 Kcal/mol, respectively. The other lone pair transitions of LP →σ* exhibited relatively low delocalization energies. The values of $E^{(2)}$ arising from LP →σ* transitions are found to be lower than those arising from LP→π* transitions due to the presence of very weak interactions between the D and A species. Such transitions LP(1)S10→σ*(C9-N11), LP(2)S10→σ*(N8-C9), LP(2)S10→σ*(C9-N11), LP(1)N11→σ*(C9-S10), LP(1)N12→σ*(C13-C18), LP(1)O20→σ*(C16-N19), LP(2)O20→σ*(C16-N19), LP(2)O20→σ*(N19-O21), LP(2)O21→σ*C16-N19), and LP(2)O21→σ*(N19-O20) were observed as taking the $E^{(2)}$ 3.61, 10.67, 14.12, 8.88, 8.63, 4.26, 13.03, 19.29, 12.93, and 19.20 Kcal/mol, respectively. As mentioned earlier, there were significant interactions between lone pair donor and anti-bonding acceptor orbitals, constructing high interaction stability, thereby inducing NLO features in the dithizone chromophore **8**.

## 3. Results and discussion

### 3.1. Evaluating thermal quantities

### 3.1.1. Thermal conductivity (K)

To evaluate the thermal conductivity (K) of fluid phase for the target nitrodithizone **8**, the selected procedure and equation 1 describing in the reference [56], are adopted to obtain K value.

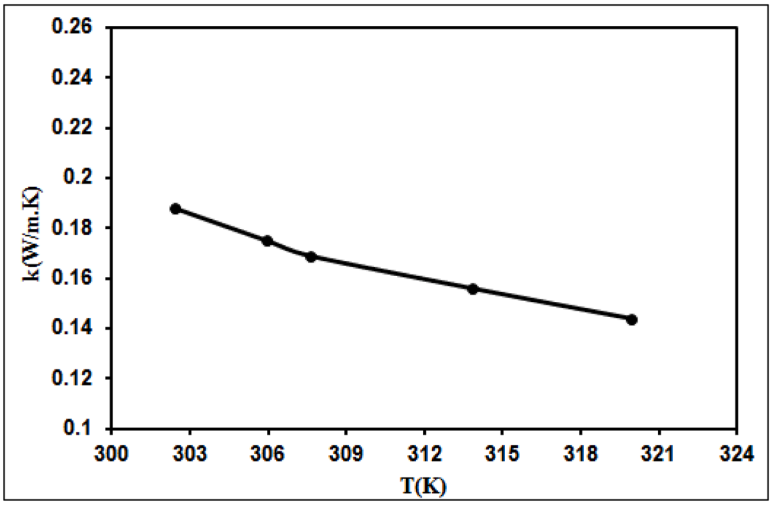

**Fig. 13.** The obtaining K value of the nitrodithizone **8** fluid at various temperatures.

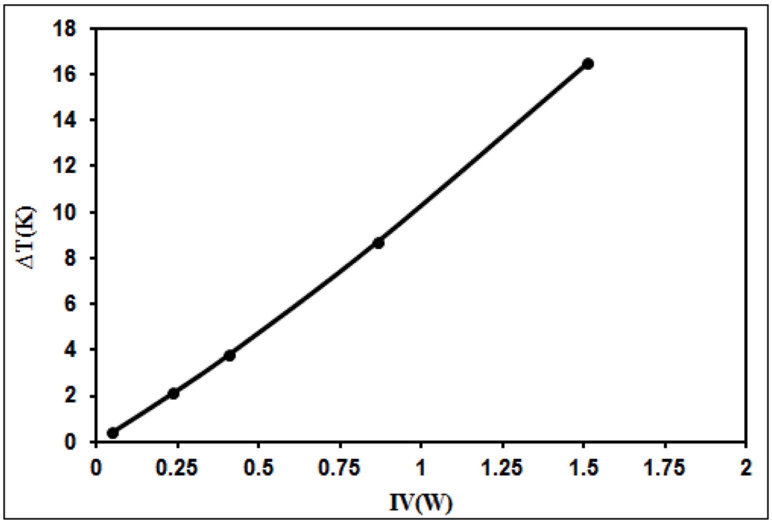

**Fig. 14.** The plot of ΔT against IV obtaining in the nitrodithizone **8** fluid.

$$K = \frac{IV\ln\left(\frac{r_2}{r_1}\right)}{2\pi h(T_1 - T_2)} \tag{1}$$

Where IV refers to the produced current and voltage for the direct current (D.C.) power supplied, h represents the height level of the cylinder used, while $r_1$ and $r_2$ correspond to the radii of the cylinders 1 and 2 at the absolute temperatures $T_1$ and $T_2$, respectively. Throughout a range of selected temperatures, all measurements were performed successfully. The results revealed that the K value of the nitrodithizone **8** solution (EtOH used as a solvent) was temperature-dependent, showing a gradual decrease due to the temperature raised as plotted in Fig. 13. In the further investigation in term of the thermal behavior of the target sample, the plotting configuration of temperature difference (ΔT) observed between the inner and outer barriers of the fluid sample and IV, is acquired as configured in Fig. 14. This plot demonstrates a positive correlation as indicating that a raise in IV leads to a corresponding raise in the temperature difference.

### 3.1.2. Viscosity (η)

By following the procedure as described in [38], the viscosity (η) of the target nitrodithizone **8** was acquired using an Ostwald viscometer according to the aforementioned reference. For the nitrodithizone **8** fluid, the η value is calculated according to the mathematical relation given in Eq. 2.

$$\frac{\eta}{\eta_o} = \frac{\rho_i t_i}{\rho_o t_o} \tag{2}$$

In this context, η and $\rho_i$ represent the viscosity and density of nitrodithizone **8** fluid respectively, while $t_i$ represents the fluid time recorded between the upper and lower points as marked in the Ostwald viscometer. Water is utilized as a standard reference with parameters $\eta_o$, $\rho_o$, and $t_o$ corresponding to its viscosity, density, and flow time. The measured $\rho_i$ and η values of nitrodithizone **8** fluid are 1103 kg/m$^3$ and $1.78 \times 10^{-3}$ Pa. sec, respectively at 29.4 °C.

### 3.1.3. Quantity of specific heat ($c_p$)

By adopting the experiment under slight modifications as given in the above reference [38], the designed calorimeter was calibrated with de-ionized water and utilized to acquire the specific heat quantity ($c_p$) of the target nitrodithizone **8**. In this experiment, an insulating-heating substance is configured around the measured glass column in order to minimize heat loss. In this mode, a DC power part was set up to be fit with a heating coil utilized as a power source. To monitor the variation in temperature factor, a digital thermometer inside an appropriate glass

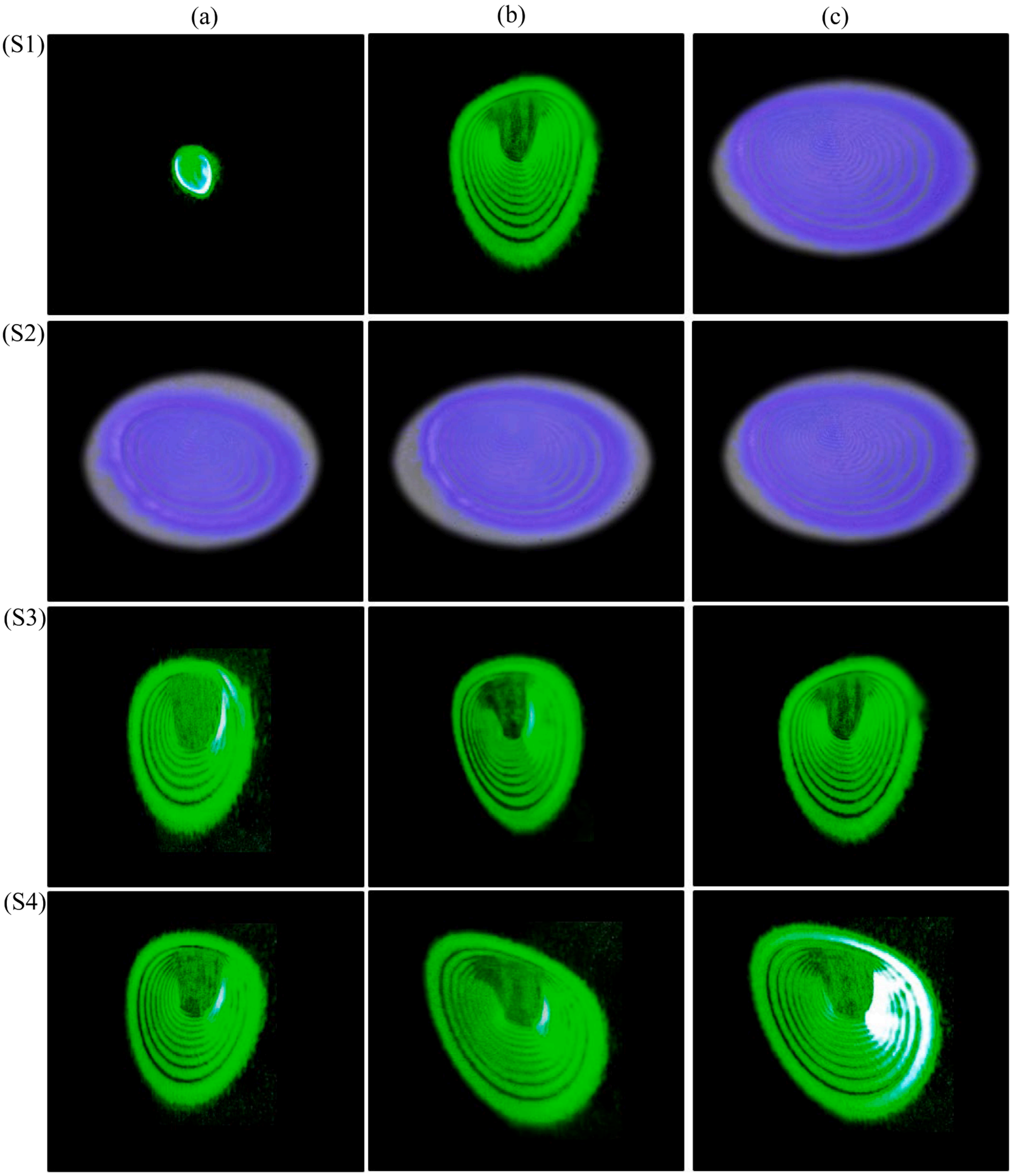

**Fig. 15.** Static AOS in the nitrodithizone **8** fluid utilizing two beams viz., 473 and 532 nm.

rod is positioned in the top area of the calorimeter, allowing to measure the temperature for the target fluid in both cases (before and after heating). The $c_p$ value of the target fluid is accurately determined upon verifying the current, voltage, and period of heating. The measured value of $c_p$ for the nitrodithizone **8** fluid was 2049 J/kg. K.

### 3.2. *NLO activity study*

#### 3.2.1. *Identification of AOS*

In the AOS experiment, two laser beams ($\lambda_1$ and $\lambda_2$) were used, one $\lambda_2 = 532$ nm as the sample has low absorption coefficient, small amount of beam energy is thus absorbed by the target sample and no DPs produced. As the medium have large absorption coefficient (at $\lambda_1 = 473$ nm), large amount of energy is therefore absorbed and the DPs produced smoothly. When both beams pass simultaneously, two types of DPs produced one due to $\lambda_1$ based on spatial self-phase modulation (SSPM) and one due to $\lambda_2$ based on cross self-phase modulation (XSPM). This effect was firstly observed and interpreted by Agrawal [57]. Fig. 15 shows the static AOS effect with $\lambda_1$: 473 and $\lambda_{2:}$ 532 nm. In Fig. 16, each beam has CW character. Meanwhile, the beam character (473 nm) is changed to pulse *via* a frequency generator due to the presence of TTL function, so that pulsed or dynamic AOS resulted. The effect noticed can be considered as a message written by the beam $\lambda_1 = 473$ nm and reads by the beam $\lambda_2 = 532$ nm, so that the beam 532 nm have no effects on the DPs resulted except at their intensity. The beam 473 nm have number of effects viz., area of DPs, number of rings, and their asymmetry noticed.

#### 3.2.2. *Identification of DPs*

In the first experiment of DPs at 56 mW, Fig. 17 shows the effect of changing convergent and divergent beam wave fronts, so that two types

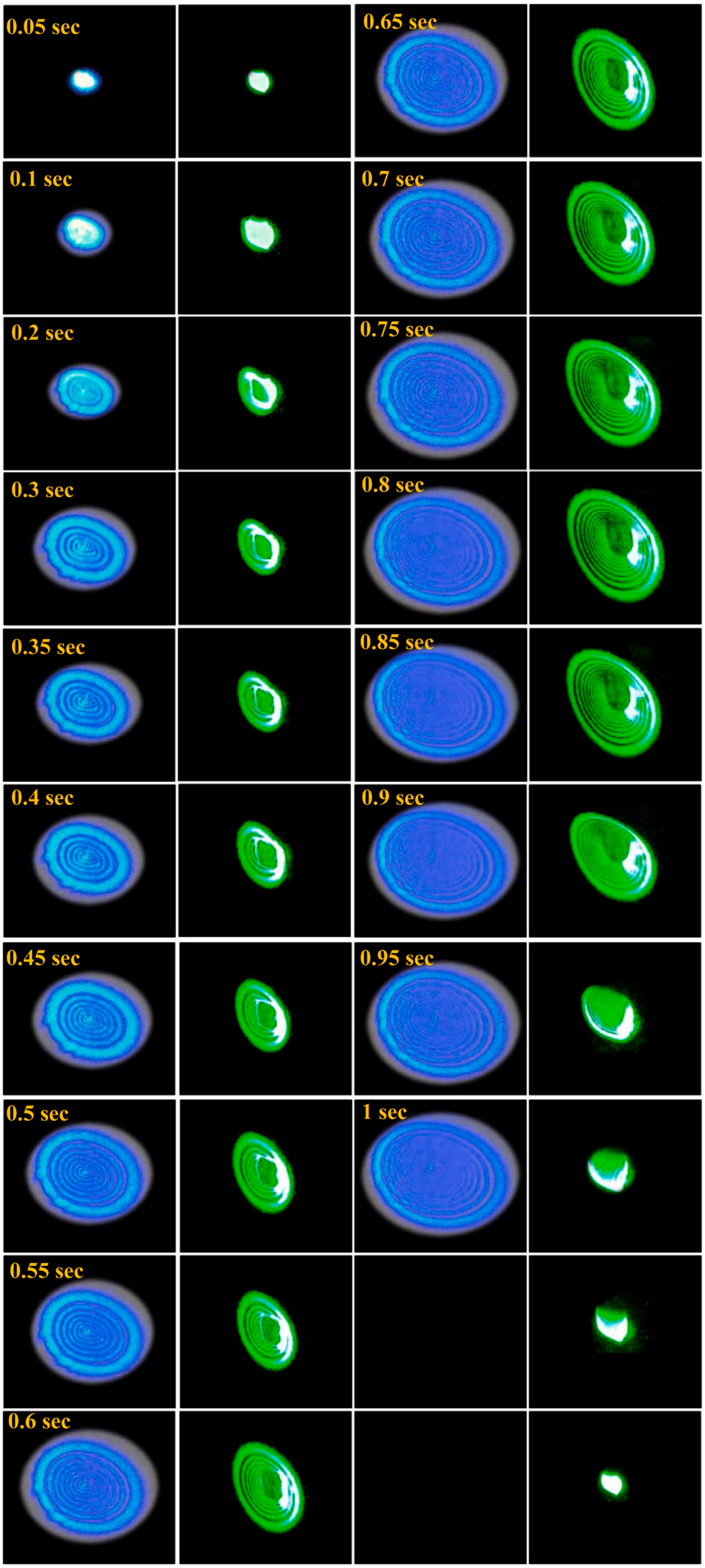

**Fig. 16.** Dynamic AOS using two beams 473 and 532 nm in the nitrodithizone **8** fluid.

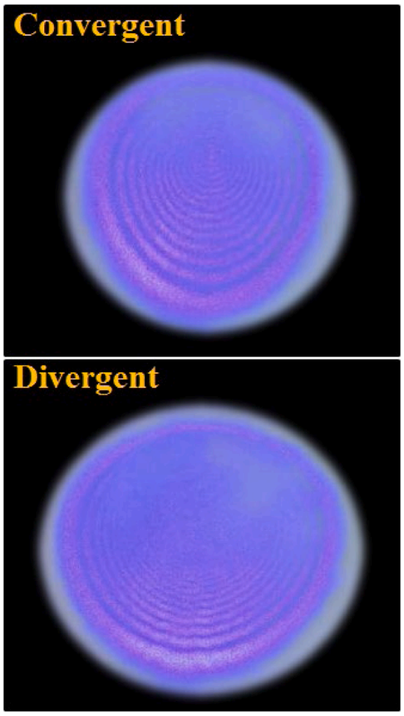

**Fig. 17.** Effect of wave front kind on the DPs in the nitrodithizone **8** fluid at power input 56 mW.

of DPs resulted. The kind of the beam wave is responsible for determining the type of DP. Such effect was first studied by Santamato and Shen in 1984 [58] and other two groups [59,60]. In case of resulted DPs depends on the interaction mode of the laser beam and target sample, such effect was extensively investigated. In the second experiment, one have the effect of power input on DPs resulted. At low input, no rings appeared as a result of low energy absorbed so that small heat resulted and small, bright, and circular spot drawn by the laser beam on the screen. By elevating the beam power, the self-defocusing (SDF) resulted causes to increase the spot area, then the spot breaks into rings. Meanwhile, the increase of the laser beam power leads to dramatically raise in the number of rings. The DPs resulted asymmetry in the x-y plane with respect to the z-direction propagation, so that the upper part of the DPs squeezed due to the thermal vertical current as such behavior shown in Fig. 18. In the laser experiment, the temporal evolution of character DPs is emerged where the beam follows the same behavior (Fig. 19) in terms of spot area and intensity squeezed of DPs increased.

Upon the laser beam passed through the sample medium, part of its energy absorbed then reradiated and the medium temperature increased in the shape of Gaussian distribution. The temperature is maximum at the z-axis and decreased away in the x-y plane. Laser heating generated from thermal energy of both conductive and convective transport. The raised heating of liquid is replaced by cool parts, conducting to an upward liquid current. As result, the both medium refractive index gradient and DPs diameter are reduced so that the DPs appeared squeezed, meanwhile their asymmetry appeared in half level as displayed in Fig. 18. With increasing power input, the number of rings increased. It is demonstrated that the interaction of the laser beam with the nonlinear medium depends on the type of beam wave front and its sign so that the different DPs resulted when the beam has convergent and divergent laser beam (see Fig. 17). The stages of the temporal development of DPs are shown in Fig. 19, referring to small spot appeared on the screen due to the low power input so that the spot area appeared equal in case of the medium is absent. By increasing the power input, the SDF effect extends the area of spot, thereby the spot split into rings whose number increased with power input increased. Ultimately, their asymmetry form appeared in the upper half of DPs.

### 3.2.3. *Calculating the nonlinear refractive index (n2)*

Throughout the application of Gaussian laser beam on the nonlinear nitrodithizone **8** fluid, the change of the phase ($\Delta\varphi$) is normally occurred due to the changes of medium refractive index ($n_2$) as a result of absorptive part of the beam energy.

N is the maximum number of rings, λ is the laser beam wavelength

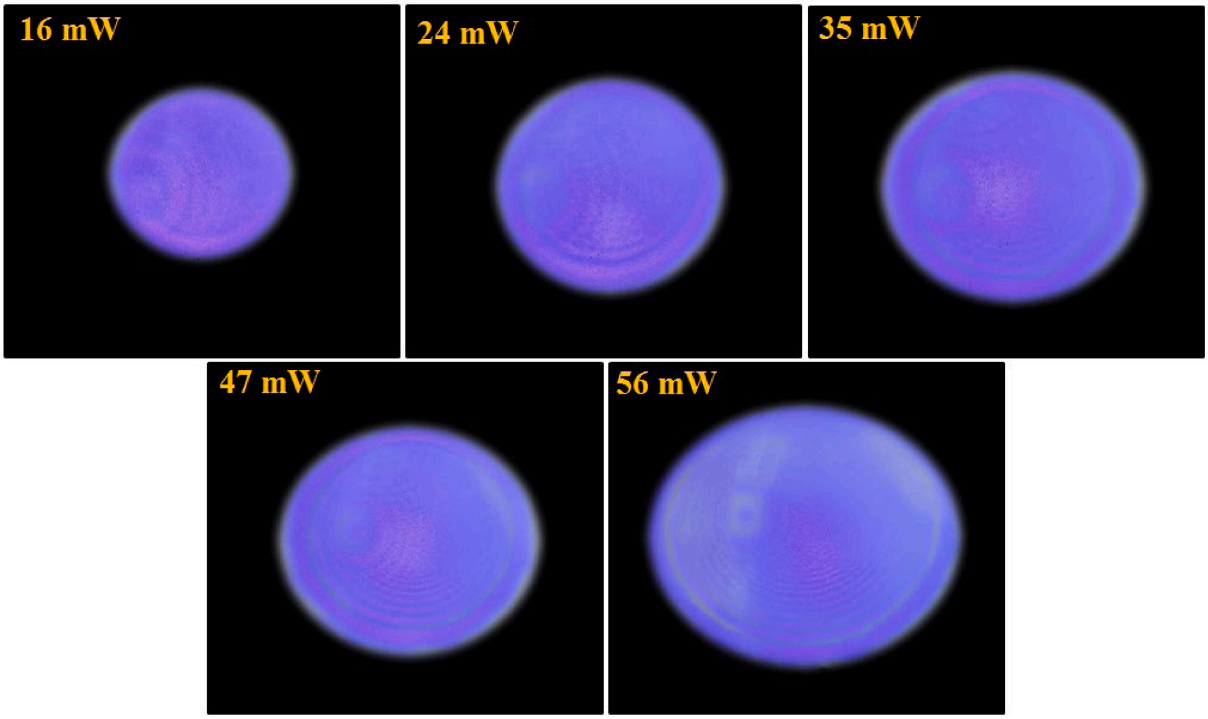

**Fig. 18.** Input effect of beam power on the DPs in the nitrodithizone **8** fluid.

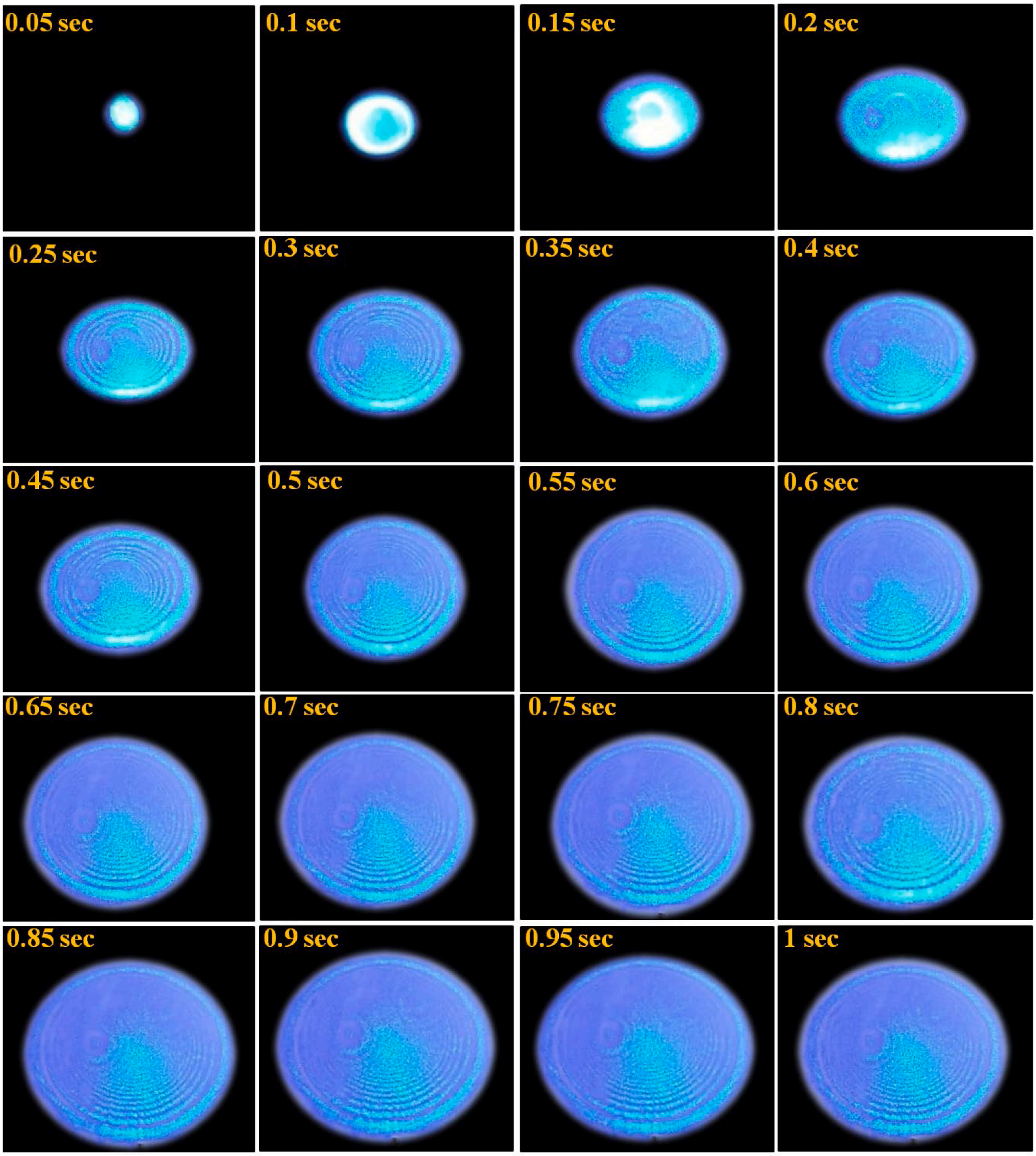

**Fig. 19.** Temporal evolution of DP resulted in the nitrodithizone **8** fluid at power input 56 mW.

and d is the sample thickness so that

$$\Delta\varphi = \Delta n k_o d e^{-\frac{2r^2}{\omega^2}} \tag{3}$$

$k_o$ is the wave vector of the laser beams, r is the distance from the beam axis and $\omega$ is beam spot size. $\Delta\varphi = \Delta\varphi_o$ refers to the phase change at a maximum level on the axis which can be written as follows:

$$\Delta\varphi_o = \Delta n k_o d \tag{4}$$

$\Delta\varphi_o$ can be written as follows:

$$\Delta\varphi_o = 2\pi N \tag{5}$$

So that the change in the medium refraction index can be written according to reference [61].

$$\Delta n = N\lambda/d \tag{6}$$

$n_2$ can be related to $\Delta n$ as follows

$$n_2 = \frac{\Delta n}{I} \tag{7}$$

I is the beam intensity and is given by

$$I = \frac{2P}{\pi\omega^2} \tag{8}$$

P is the maximum power input.

For N=10, $\omega = 19.235$ μm, P = 56 mW, d = 0.1 cm and λ = 473 nm so that $\Delta n = 4.73 \times 10^{-3}$ and $n_2 = 4.901 \times 10^{-7}$ cm$^2$/W.

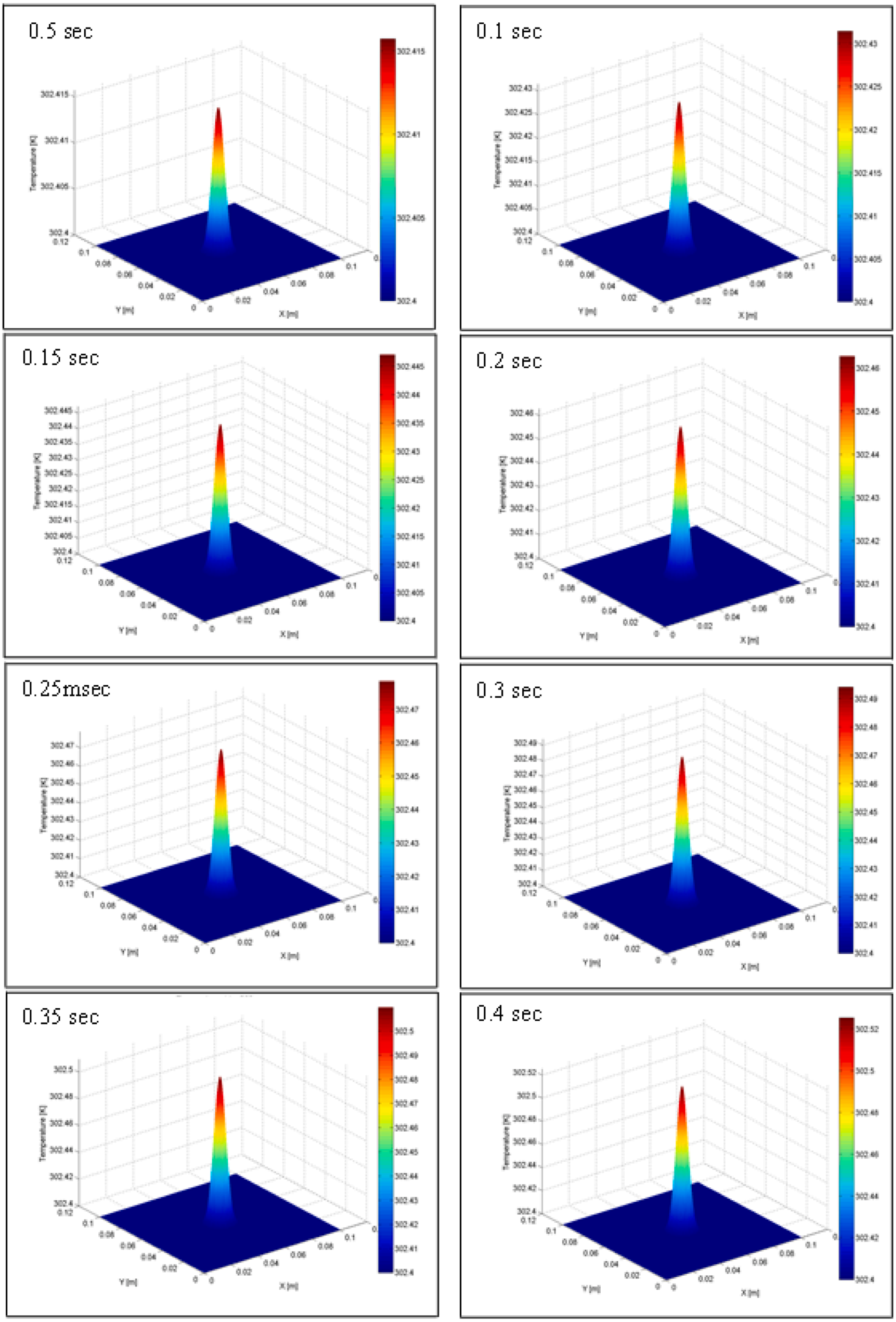
0.5 sec
0.1 sec
0.15 sec
0.2 sec
0.25msec
0.3 sec
0.35 sec
0.4 sec

**Fig. 20.** The simulation models of heat diffusion of the nitrodithizone **8** fluid under laser beam irradiation.

A comparative study in term of nonlinear refractive index ($n_2$) values between the nitrodithizone **8** and other related compounds including a standard reference, is developed. Such efficient value of $n_2$ ($4.901 \times 10^{-7}$ cm$^2$/W) compared to the values of studied substances addressed in

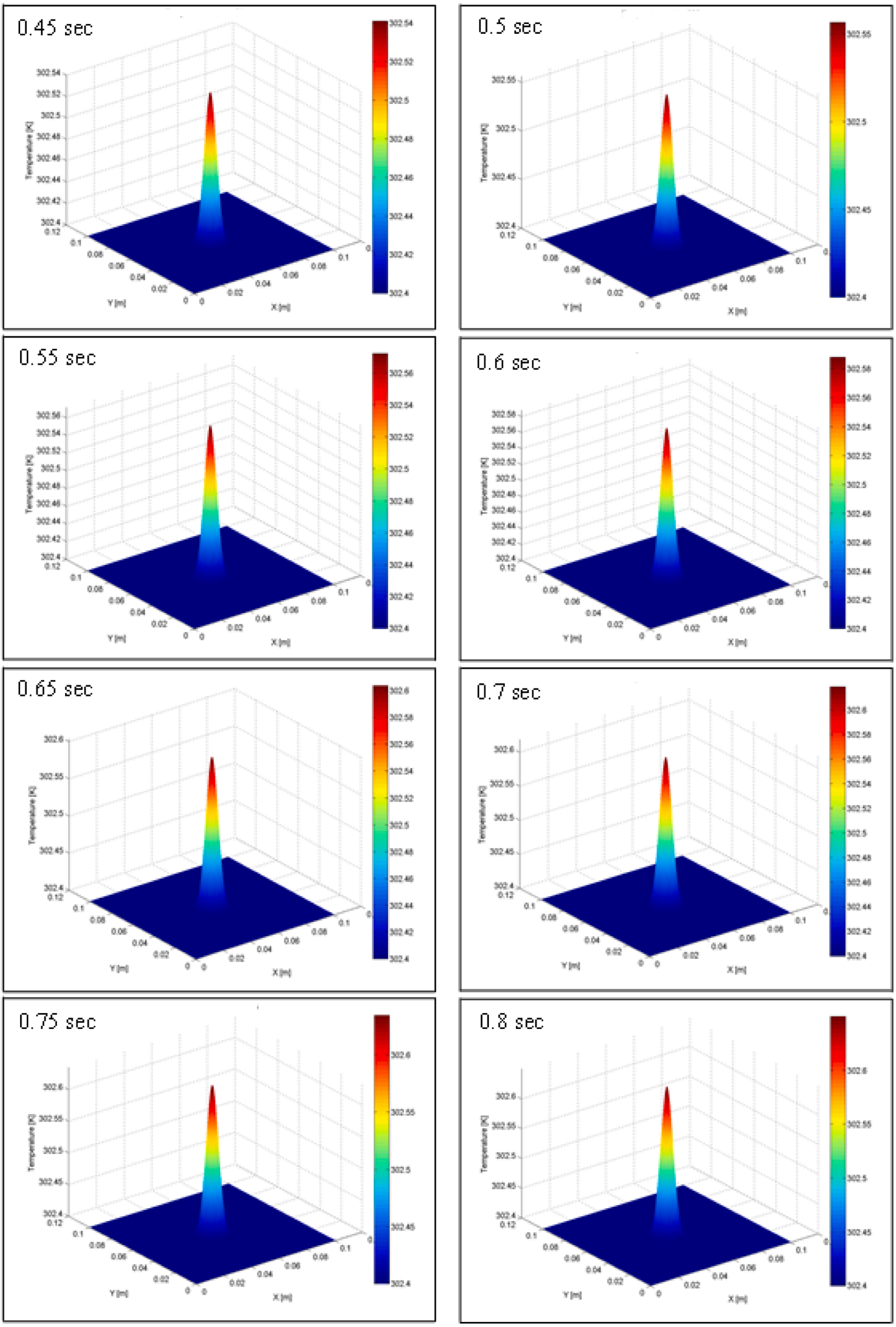

Fig. 20. (*continued*).

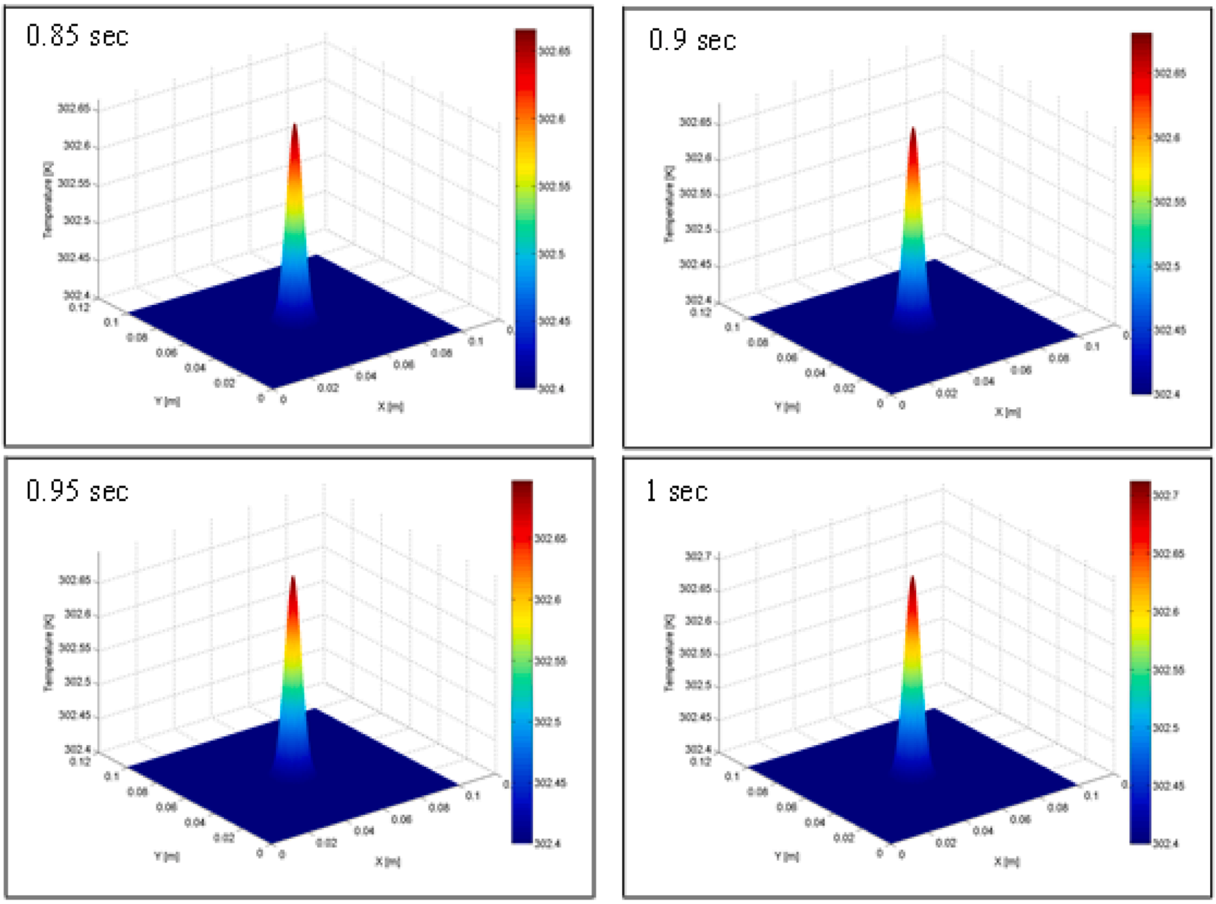

**Fig. 20.** (*continued*).

previous works [62–65], suggests that the target nitrodithizone **8** may be invested as a promising optical limiter or optical switching in the low-power laser.

## 4. Simulation models

### 4.1. Simulating thermal diffusion

In simulating model, a Finite Difference Method (FDM) is numerically conducted to solve the 2D-transient heat conduction equation integrated with a heat source [66]. This context discloses that a continuous wave (CW) laser beam acts as an internal heat source cooperated with the target fluid (nitrodithizone **8**). The partial differential equation is used to conduct the temporal and spatial distribution of temperature factor throughout the target fluid as represented in Eq. 9 [66]. It is noteworthy that the aforementioned equation is considered as a fundamental component for thermal analysis with many broad applications in physics, engineering, and materials science.

$$\frac{\partial \mathrm{T}(\mathrm{x},\mathrm{y},\mathrm{t})}{\partial \mathrm{t}} = \alpha\left(\frac{\partial^2 \mathrm{T}(\mathrm{x},\mathrm{y},\mathrm{t})}{\partial \mathrm{x}^2} + \frac{\partial^2 \mathrm{T}(\mathrm{x},\mathrm{y},\mathrm{t})}{\partial \mathrm{y}^2}\right) + \mathrm{Q}(\mathrm{x},\mathrm{y},\mathrm{t} \tag{9}$$

Where $\mathrm{T}(\mathrm{x},\mathrm{y},\mathrm{t})$ represents the temperature field as a function of space and time. $\frac{\partial \mathrm{T}}{\partial \mathrm{t}}$ represents the first partial derivative of temperature according to time. $\frac{\partial^2 \mathrm{T}}{\partial \mathrm{x}^2}$ *and* $\frac{\partial^2 \mathrm{T}}{\partial \mathrm{y}^2}$ are the second spatial derivative components in the x and y directions, respectively. The thermal diffusion is identified as $\alpha$. $\mathrm{Q}(\mathrm{x},\mathrm{y},\mathrm{t})$ represents the rate of temperature increase per second.

The results disclose when the laser beam positions directly at the material center, the consequential heat localized in a diffused manner. This heat diffusion for the target fluid is predominantly organized throughout its thermal diffusivity. The practical thermal diffusivity of the nitrodithizone **8** fluid was determined and found to equals 0.83 × $10^{-7}$ $m^2/s$. The laser beam used in the thermal model has a power output of 56 mW. Temperature measurements were recorded at 50 millisecond intervals for a total period per one second as configured in Fig. 20. By one second timing, the temperature due to laser irradiation increased approximately 0.3 °C. In comparison with the theoretical simulations, the temperature will be raised to 0.31 °C in order to validate the thermal quantities such as $c_p$ and density for the target fluid under the same applied laser power and time. Heat is transmitted mechanically in the liquids through the translational motion of molecules. Upon irradiating the localized region by a laser beam, the molecules in this region absorbed energy, thereby increasing their kinetic energies and enhancing their random translational velocities. The excess energetic molecules collide with cooler neighboring molecules, thereby transferring a portion of their kinetic energies. Rotational and vibrational motions of the molecules may also contribute to energy exchange even occurred in a low extent. This process occurs continuously among a high number of molecules, resulting in the gradual transfer of thermal energy from the hotter region to the surrounding cooler regions. Consequently, the raised temperature is diffused into the target liquid not only through the molecules movements over large distances, but also through successive molecular collisions and the energy transfer between them. The high consistency obtained between the experimental and theoretical values highlights the validity and reliability of the selected simulation model.

### 4.2. Simulating the DPs

Throughout the Gaussian laser beam propagated in a nonlinear

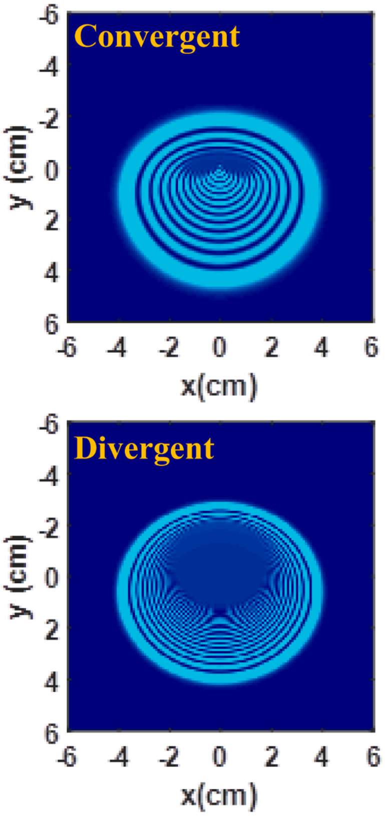

**Fig. 21.** The simulation of the DPs of the laser beam for two laser beams viz., convergent and divergent of 56 mW passing through nitrodithizone **8** fluid.

medium (having intensity- dependent refractive index and absorption coefficient), the DPs are generated as shown in section 3.2.2. Their area, ring numbers, and asymmetry raise with an increase of incident beam power and depend on beam wave front type and time variation. If the beam radius is $\omega$, its wave front radius (R), its wavelength ($\lambda$), its wave vector (k), and beam power (P), the complex amplitude $E(x,y,t,z=0)$ at the entryway of the sample medium that extend a distance, d, can be written as follows [67,68]:

$$E(x,y,t,z=0)=\left(\frac{2P}{\pi\omega^2}\right)^{1/2}\exp\left(-\frac{x^2+y^2}{\omega^2}\right)\exp\left(-ik\frac{x^2+y^2}{2R}\right) \tag{10}$$

The laser beam phase $\Delta\varphi(x,y,t)$ at the medium exit plane can be written as follows:

$$\Delta\varphi(x,y,t)=\frac{2\pi}{\lambda}d[n(x,y,t)-n(0,0,t)] \tag{11}$$

The refractive index of the target medium, $n(x,y,t)$ can be expressed as follows:

$$n(x,y,t)=n_o+\frac{dn}{dT}\Delta T(x,y,t) \tag{12}$$

$n_o$ is the medium linear refractive index, $\frac{dn}{dT}$ is the thermoptic coefficient and $\Delta T(x,y,t)$ is temperature profile increase so that the laser beam integrated complex amplitudes can be written as follows:

$$E(x,y,t,z=0)=\left(\frac{2P}{\pi\omega^2}\right)^{1/2}\exp\left(-\frac{\alpha d}{2}\right)\exp\left(-\frac{(x^2+y^2)}{\omega^2}\right)\exp\left(-ik\frac{(x^2+y^2)}{2R}\right)\exp(i\Delta\varphi(x,y,t)) \tag{13}$$

$\alpha$ is the medium absorption coefficient at wavelength $\lambda$.

The DPs on the screen distance (L) from the sample exit plane where the spatial coordinates x and y become $x', y'$ so that

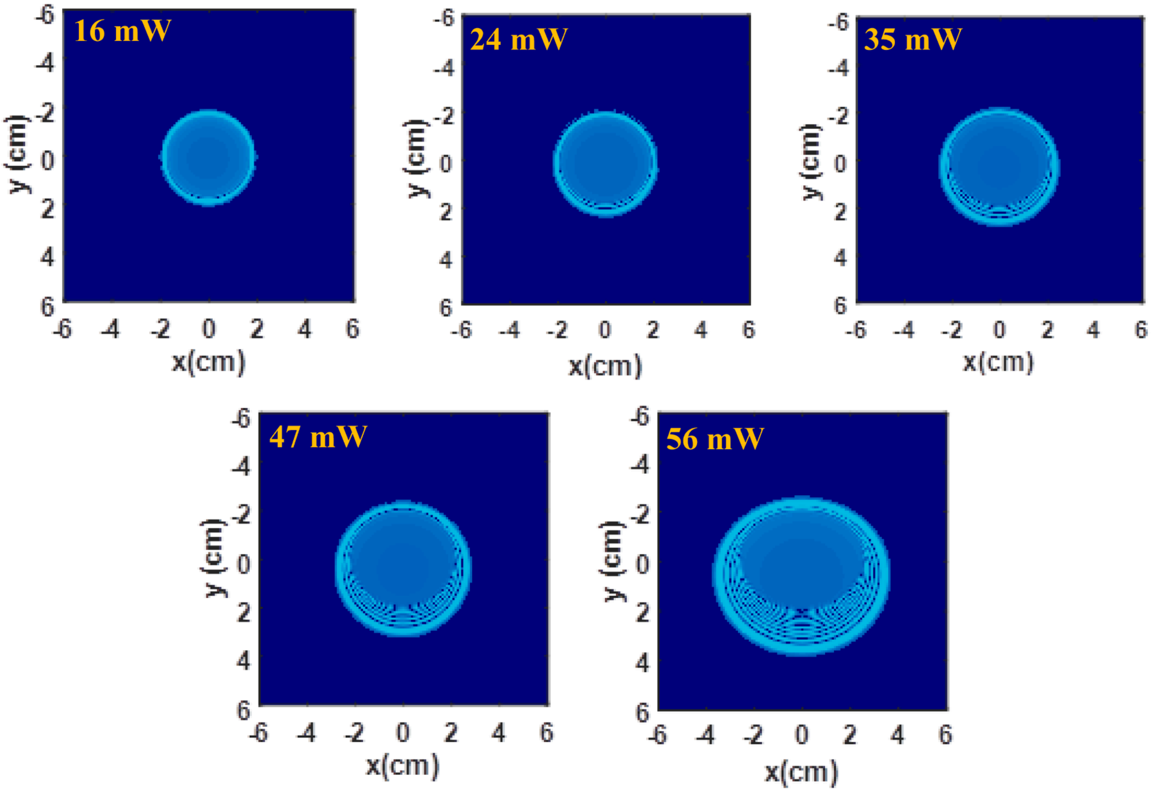

**Fig. 22.** The simulation of the DPs at different power input of the laser beam in the nitrodithizone **8** fluid.

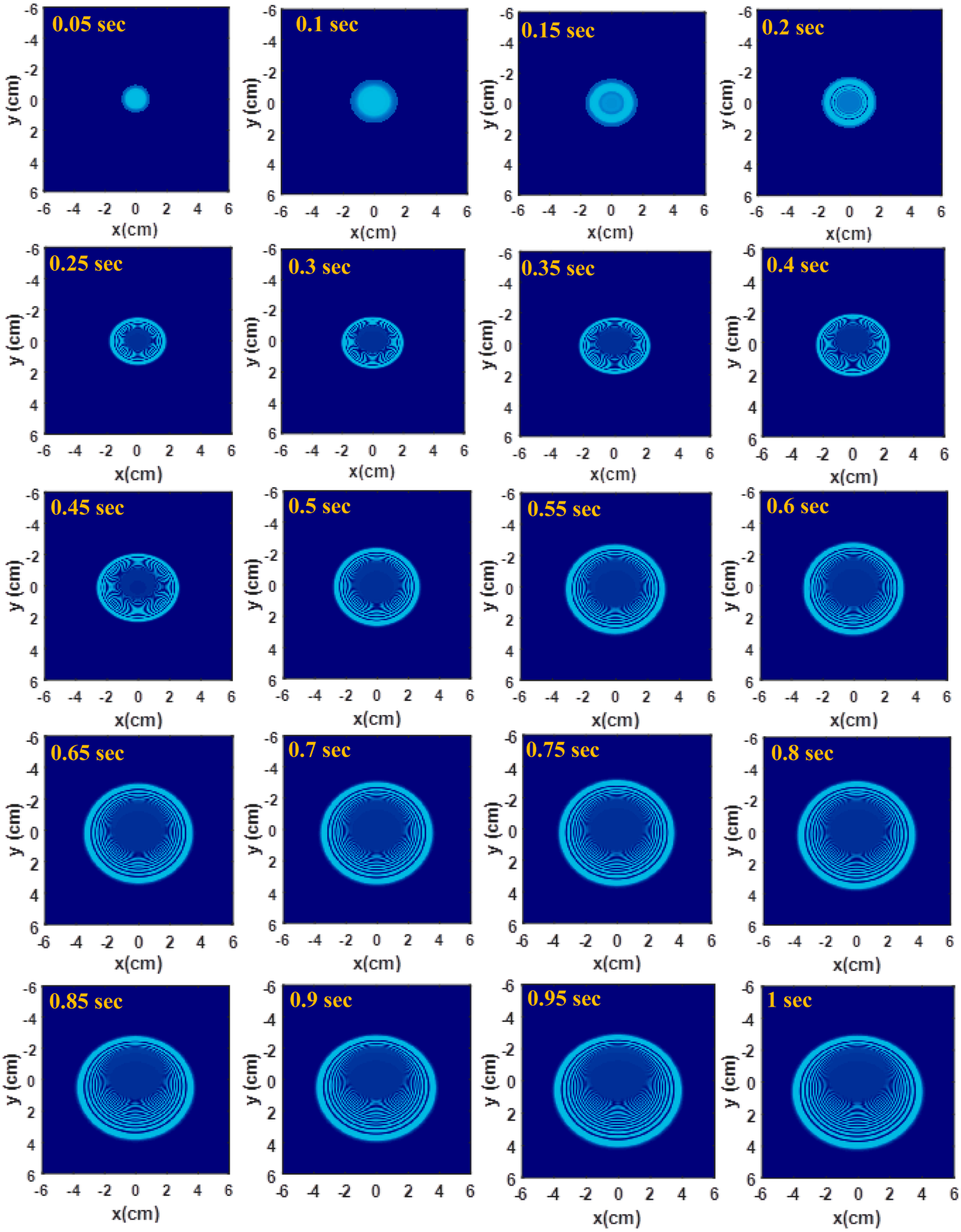

**Fig. 23.** The simulation of the DPs images (temporal evolution) at 56 mW laser beam passing through nitrodithizone **8** fluid.

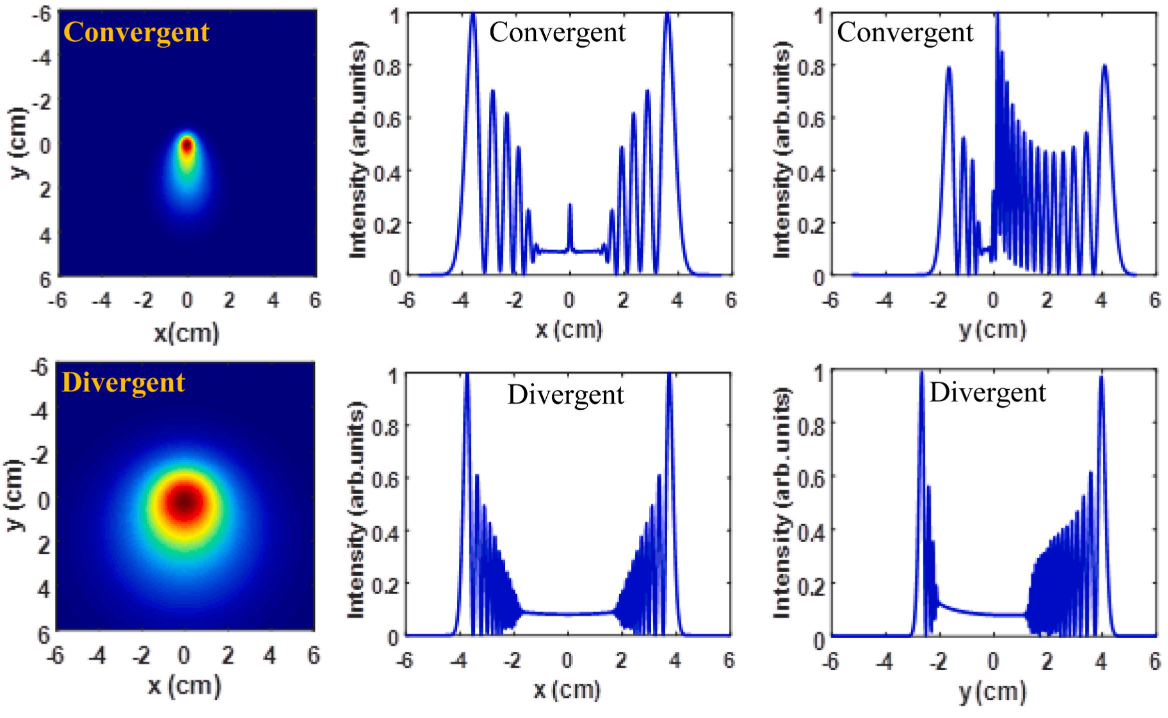

(LC) (MC) (RC)

**Fig. 24.** The simulation of (LC) 2d distribution of beam phase, 1d beam intensity distribution (MC) against x-axis and (RC) against y-axis for convergent and divergent beams at 56 mW in nitrodithizone **8** fluid.

$$E(x',y',t)=\left(\frac{2P}{\pi\omega^2}\right)^{1/2}\frac{i\pi\omega^2}{\lambda L}\exp(ikL)\exp\left(-\frac{\alpha d}{2}\right)\int_{-\infty}^{\infty}dx\int_{-\infty}^{\infty}dy.\exp\left(-\frac{x^2+y^2}{\omega^2}\right).\exp\left[\left\{-k\frac{x^2+y^2}{2R}+\Delta\varphi(x,y,t)\right\}\right].\exp\left(-ik\frac{xx'+yy'}{L}\right) \tag{14}$$

After using the Fraunhofer approximation of the Fresnel–Kirchhoff integral. The beam intensity, $I(x',y',t)$ at the screen can be written as follows:

$$I(x',y',t)=\left|\left(\frac{2P}{\pi\omega^2}\right)^{1/2}\frac{i\pi\omega^2}{\lambda L}\exp(ikL)\exp\left(-\frac{\alpha d}{2}\right)\int_{-\infty}^{\infty}dx\int_{-\infty}^{\infty}dy.\exp\left(-\frac{x^2+y^2}{\omega^2}\right).\exp\left[i\left\{-k\frac{x^2+y^2}{2R}+\Delta\varphi(x,y,t)\right\}\right].\exp\left(-ik\frac{xx'+yy'}{L}\right)\right|^2 \tag{15}$$

Mat Lab system was conducted to solve Eq. 15 numerically and the results are depicted in Figs. 21 and 22. These figures show the effect of the beam wave front kind i.e., convergent, divergent, and different laser powers on the DPs at 56 mW. Temporal evolution of the diffraction patterns emerged at 56 mW in the nitrodithizone **8** fluid is shown in Fig. 23. Figs. 24–26 show the effect of beam wave front kind on the 2d variation of beam phase (LC) and 1d variation of beam intensity against (MC) x-axis and (RC) y-axis temporal evolution at 56 mW in nitrodithizone **8** fluid. In the experimental results, comparative studies in terms of the effect of beam wave front kind, effect of beam power, and the temporal evolution of DPs, are given in Figs. 17–19. Comparing with those numerically obtained, reasonable agreement can be noticed in the number of rings, area of DPs, and shape of DPs, particularly in their squeezed form.

## 5. Conclusions

This work describes an efficient synthesis of a new unsymmetrical dithizone chromophore **8** involving a thiocarbazone linker presents as a channel between its components in its molecular architecture. The computational consequences in terms of the narrowest band gap (HOMO–LUMO) and higher values of polarizability and first hyperpolarizability indicate high nonlinear behavior for the synthesized nitrodithizone chromophore **8**. The effective electronic behavior of nitrodithizone chromophore **8** demonstrated by theoretical and practical experiments, is highly expected due to the presence of $NO_2$ substituent as a potent acceptor group, demonstrating greater internal charge transfer (ICT) through the entire π-system of the entitled chromophore **8**. The passage of two CW continuous wave laser beams have led to the generation of diffraction patterns (DPs), one directly obtained and one obtained *via* the cross self-phase modulation (XSPM). Upon the DPs generated with high-quality nonlinear optical (NLO) activity was evaluated, the nonlinear refractive index (NLRI) and all-optical switching (AOS) properties were identified using two CW laser beams. Our results underscored that the synthesized nitrodithizone **8** exhibited good NLO response, making it a promising candidate for further investment in non-linear optics.

## CRediT authorship contribution statement

**Amir Hussein Ali:** Software, Methodology, Formal analysis. **Ahmed Majeed Jassem:** Writing – review & editing, Writing – original draft, Validation, Methodology, Investigation, Formal analysis. **H.A. Sultan:** Visualization, Software, Resources. **Qusay M.A. Hassan:** Visualization, Resources, Methodology, Formal analysis, Data curation. **C.A. Emshary:** Writing – review & editing, Validation, Project administration, Methodology, Conceptualization. **Wisam A. Radhi:** Visualization, Software, Resources.

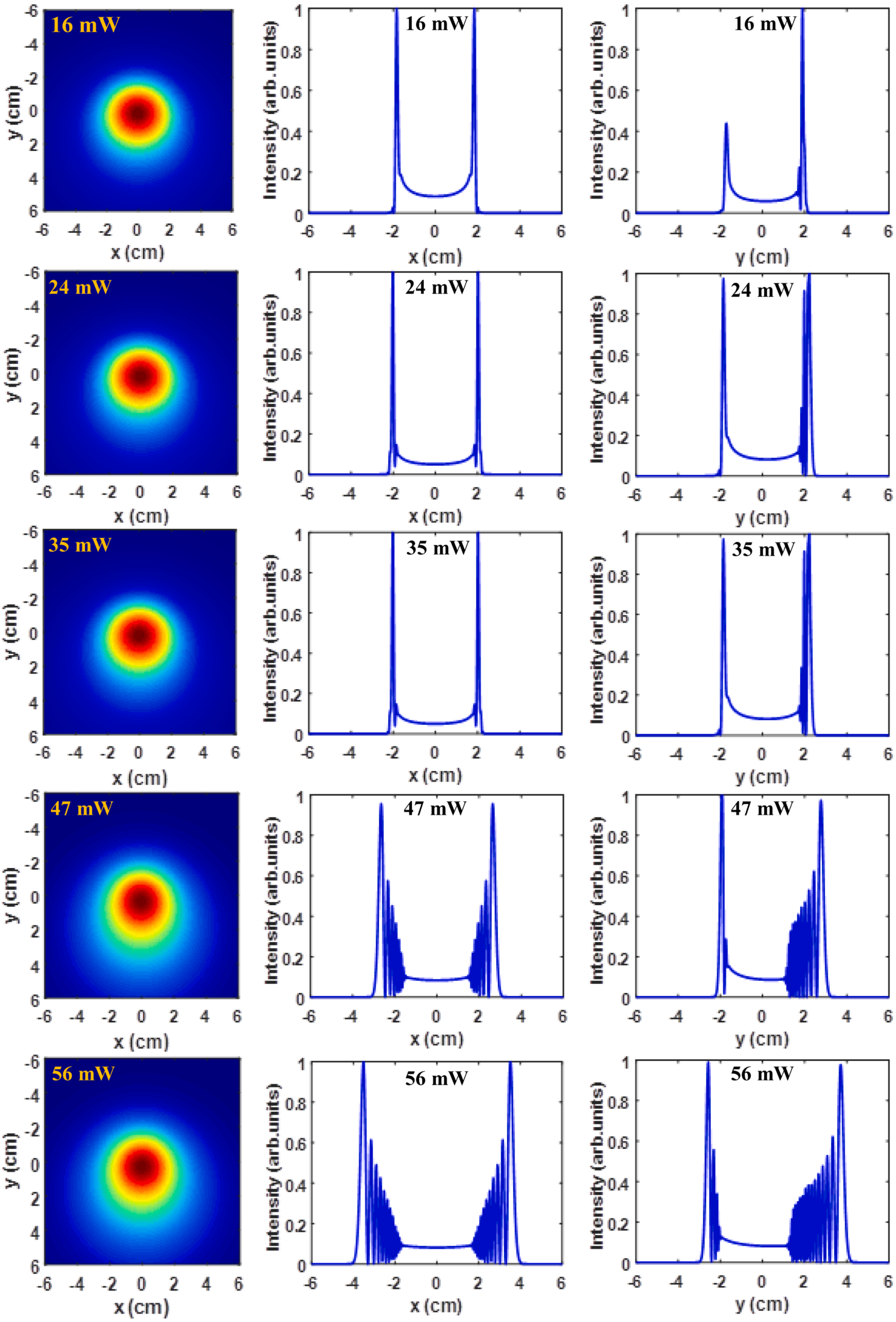

(LC) (MC) (RC)

**Fig. 25.** The simulation of (LC) 2d distribution of beam phase, 1d beam intensity distribution (MC) versus x-axis and (RC) versus y-axis for power input in nitrodithizone **8** fluid.

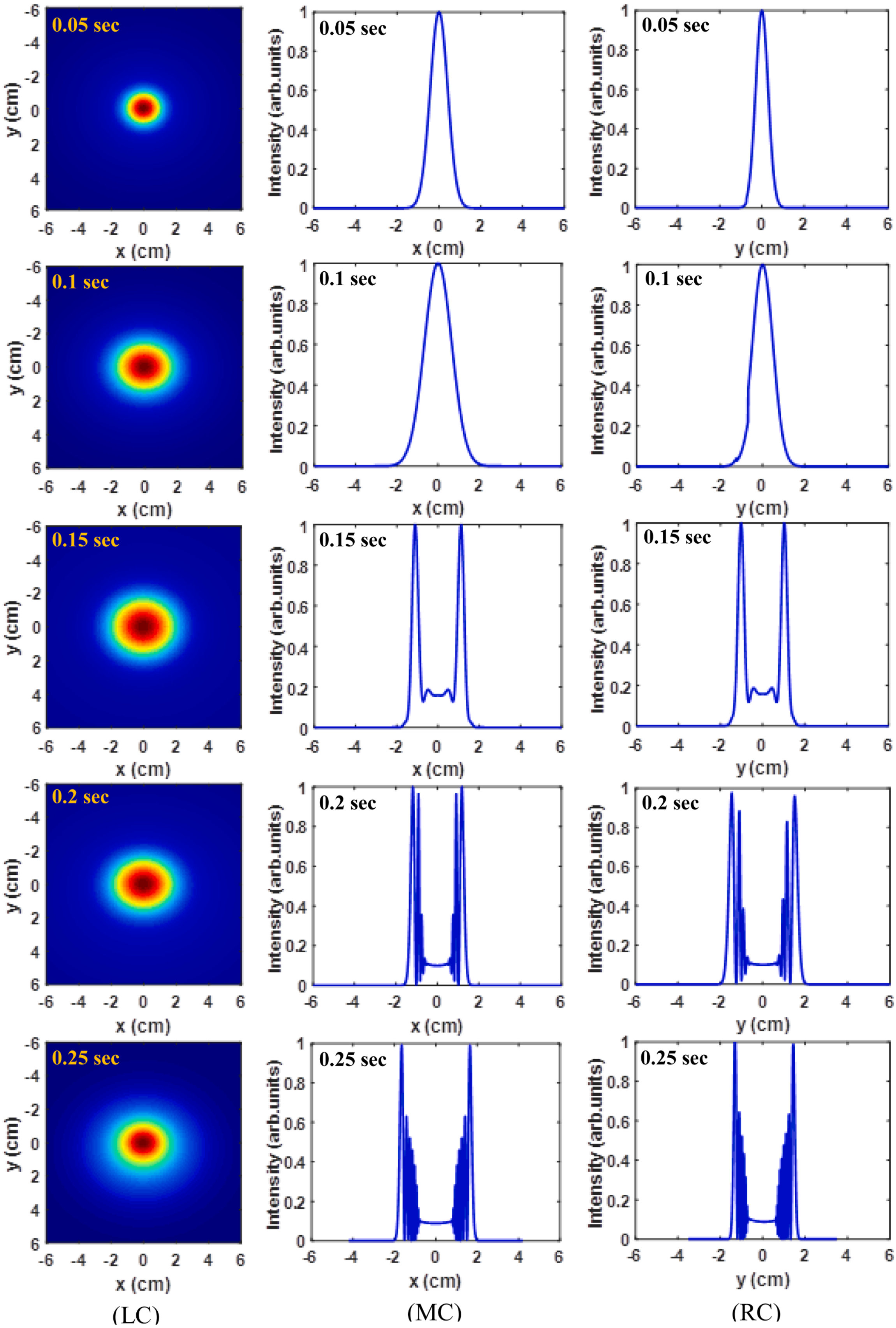

**Fig. 26.** The simulation of temporal evolution of (LC) 2d distribution of beam phase, 1d beam intensity distribution (MC) versus x-axis and (RC) versus y-axis at 56 mW in nitrodithizone 8 fluid.

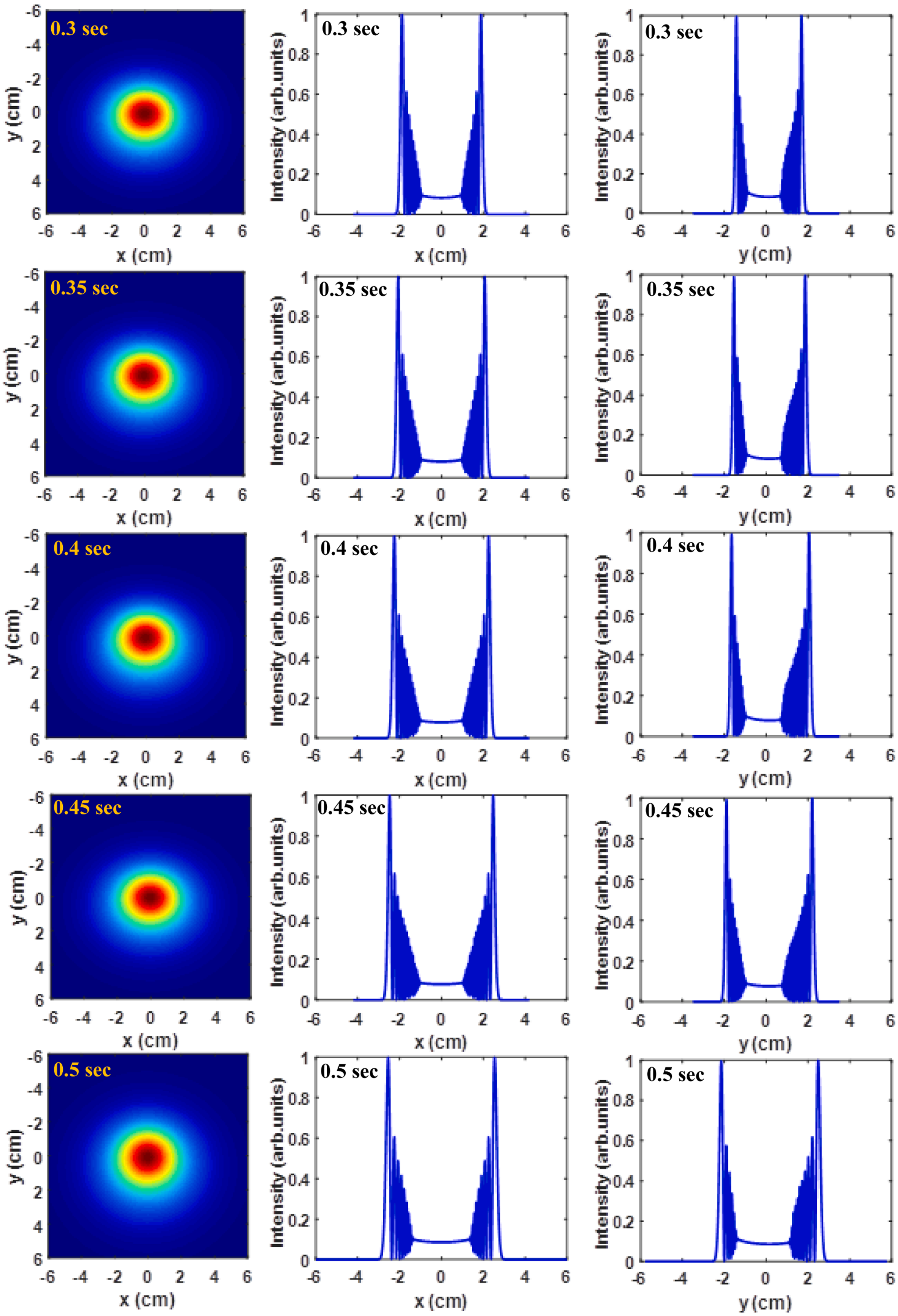

(LC) (MC) (RC)

**Fig. 26.** (*continued*).

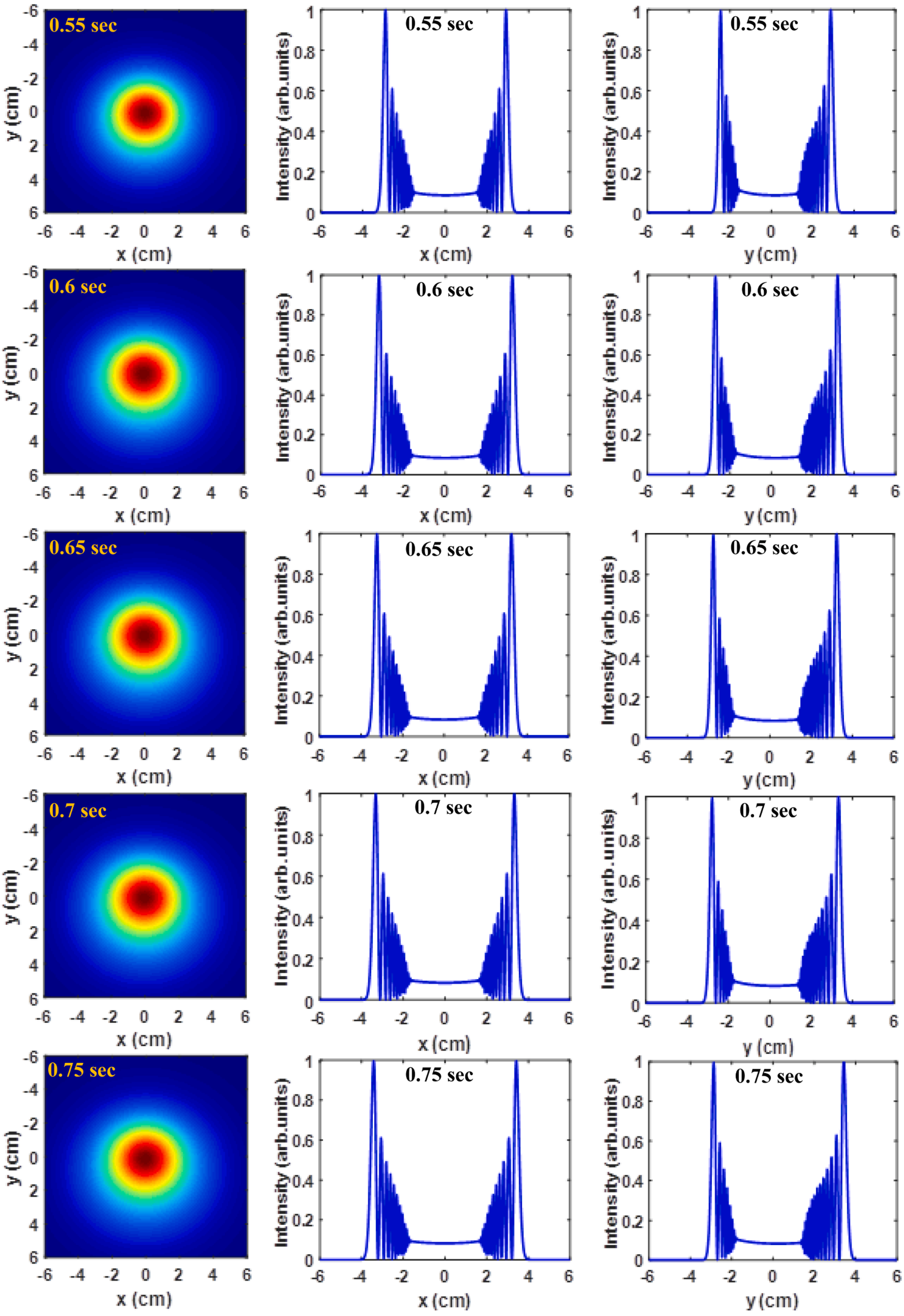

(LC) (MC) (RC)

**Fig. 26.** (*continued*).

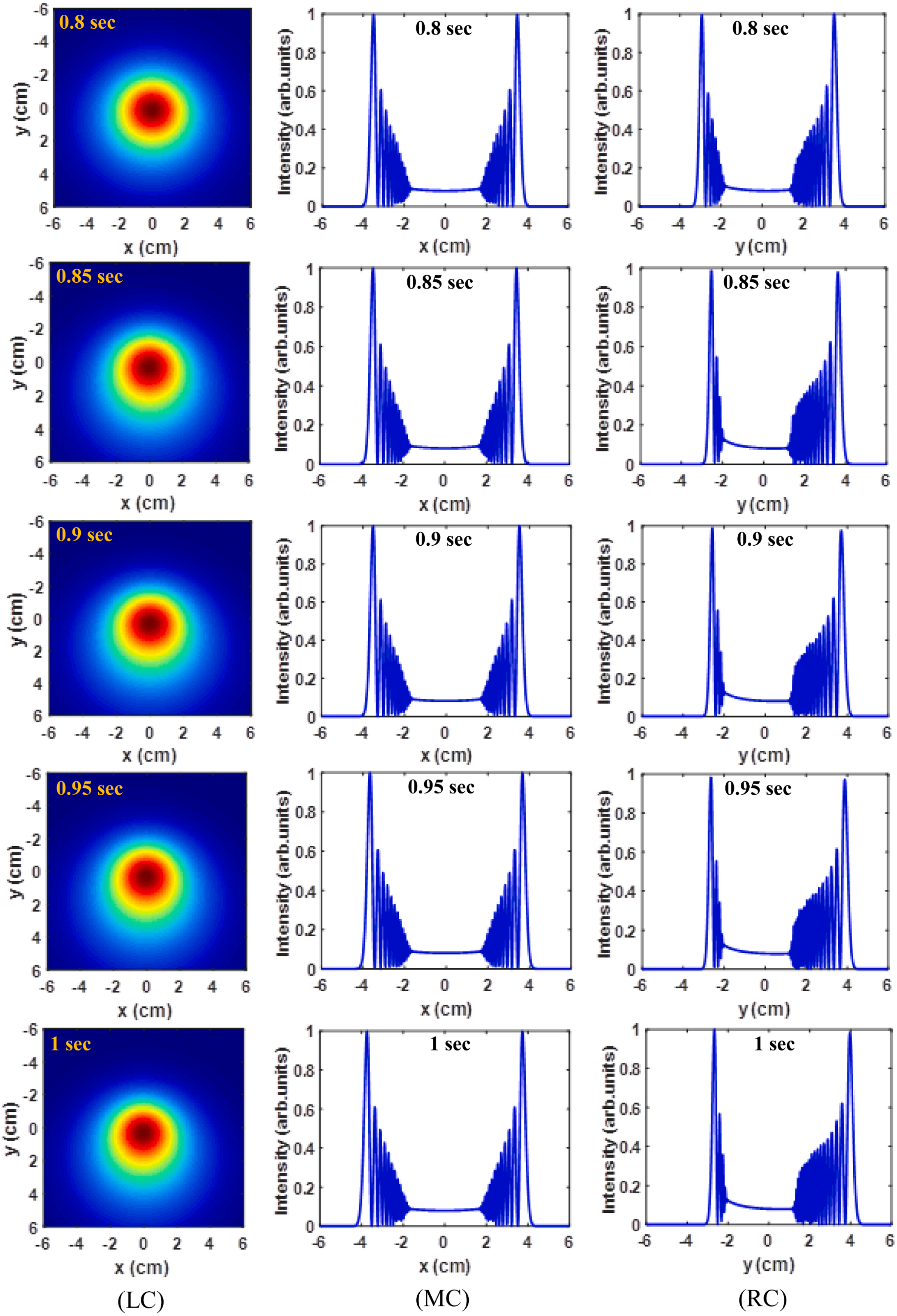

**Fig. 26.** (*continued*).

## Declaration of competing interest

The authors declare the following financial interests/personal relationships which may be considered as potential competing interests:

## Data availability

No data was used for the research described in the article.

## References

[1] A.M. Jassem, Qusay M.A. Hassan, F.A. Almashal, H.A. Sultan, A.M. Dhumad, C. A. Emshary, L.T.T. Albaaj, Spectroscopic study, theoretical calculations, and optical nonlinear properties of amino acid (glycine)-4-nitro benzaldeyhyde-derived Schiff base, Opt. Mater. 122 (2021) 111750.

[2] R.S. Jassas, O.A. Omran, A. Abdou, M.S. Kamel, Z. Moussa, A. Abd-El-Aziz, N. Ma, H.M. Altass, A.S. Khder, E.M. Hussein, Design and DFT calculations of optoelectronic material based on thiazolobenzimidazole-coupled isatin derivatives, Mater. Chem. Phys. 325 (2024) 129689.

[3] A.M. Jassem, Qusay M.A. Hassan, C.A. Emshary, H.A. Sultan, F.A. Almashal, W. A. Radhi, Synthesis and optical nonlinear properties performance of azonaphthol dye, Phys. Scr. 96 (2020) 025503.

[4] J.K. Salim, Qusay M.A. Hassan, A.M. Jassem, H.A. Sultan, A.M. Dhumad, C. A. Emshary, An efficient ultrasound-assisted CH3COONa catalyzed synthesis of thiazolidinone molecule: theoretical and nonlinear optical evaluations of thiazolidinone-Schiff base derivative, Opt. Mater. 133 (2022) 112917.

[5] M. Tahir, H. Aftab, I. Shafiq, M. Khalid, S. Haq, A.F. El-Kott, M.A. Zein, U. Hani, Z. Shafiq, Synthesis, characterization and NLO properties of 1, 4-phenylenediamine-based Schiff bases: a combined theoretical and experimental approach, 14, RSC advances, 2024, pp. 4221–4229.

[6] A.M. Jassem, Qusay M.A. Hassan, A.M. Dhumad, H.A. Sultan, J.K. Salim, C. A. Emshary, A green ultrasound-promoted synthesis, experimental, theoretical, and nonlinear optical properties studies of benzylidenehydrazono thiazolidin-4-one derivative, Chem. Pap 78 (2024) 1849–1861.

[7] M.G. Kuzyk, Using fundamental principles to understand and optimize nonlinear-optical materials, J. Mater. Chem. 19 (2009) 7444–7465.

[8] G.S. Yaqoob, Qusay M. Hassan, A.M. Jassem, H.A. Sultan, A.M. Dhumad, C. A. Emshary, Isatin-indole hybrid molecule: A simple synthesis to design an efficient NLO material, Opt. Mater. 149 (2024) 114983.

[9] S.M. Hassan, A.M. Jassem, Qusay M.A. Hassan, H.A. Sultan, A.M. Dhumad, C. A. Emshary, Design, DFT, experimental, and NLO studies of a new hybrid containing 1, 3, 4-oxadiazole and indole moieties, Phys. Scr. 100 (2024) 015219.

[10] A. Datta, S.K. Pati, Dipole orientation effects on nonlinear optical properties of organic molecular aggregates, J. Chem. Phys 118 (2003) 8420–8427.

[11] Z. Sainudeen, P.C. Ray, Nonlinear optical properties of ionic NLO chromophores: An attempt to bridge the gap between computation and experiment, Int. J. Quantum Chem 105 (2005) 348–358.

[12] C.B. De Araújo, A.S. Gomes, G. Boudebs, Techniques for nonlinear optical characterization of materials: a review, Rep. Prog. Phys. 79 (2016) 036401.

[13] A. Muala Dhumad, Qusay M.A. Hassan, A.M. Jassem, H.A. Sultan, I.M. Jasim, C. A. Emshary, Sonochemical-Promoted multicomponent synthesis of a new amidoalkyl naphthol derivative catalyzed by [(Msim) Cl] ionic liquid and assessment of its nonlinear optical properties, ChemistrySelect 9 (2024) e202305072.

[14] M.S. Oliveira, A.B. Santos, T.V. Ferraz, G.L. Moura, E.H. Falcão, Non-symmetrical 1, 3, 4-oxadiazole derivatives: synthesis, characterization, and computational study of their optical properties, Chem. Phys. Impact 6 (2023) 100162.

[15] B. Derkowska-Zielinska, M. Barwiolek, C. Cassagne, G. Boudebs, Nonlinear optical study of Schiff bases using Z-scan technique, Opt. Las. Technol. 124 (2020) 105968.

[16] N. Kosar, S. Kanwal, H. Sajid, K. Ayub, M.A. Gilani, K.E. Ibrahim, M.K. Gatasheh, Y. S. Mary, T. Mahmood, Frequency-dependent nonlinear optical response and refractive index investigation of lactone-derived thermochromic compounds, J. Mol. Graphics. Modell. 126 (2024) 108646.

[17] J. Liu, M. Zhang, W. Gao, A. Fedorchuk, I. Kityk, Synthesis and nonlinear optical properties of novel conjugated small molecules based on indole donor, J. Mol. Struct. 1165 (2018) 223–227.

[18] I. Manikandan, M.V. Perumal, K. Jayamoorthy, Synthesis, characterization, physico-chemical and DFT studies of potential organic NLO materials: experimental and theoretical combined study, Silicon 11 (2019) 425–435.

[19] P. Chandola, J. Dwivedi, M.C. Jamali, Non-linear optical activity and biological evaluation of organic compounds by experimental and theoretical techniques, Eur. Chem. Bull. 12 (2023) 19608–19619.

[20] T. Sutradhar, A. Misra, Enhancement of nonlinear optical properties of indole based dyes through electron acceptor and π-linker for dye-sensitized solar cell applications, ChemistrySelect 4 (2019) 3697–3705.

[21] I. Biaggio, The appeal of small molecules for practical nonlinear optics, Chem. Eur. J. 28 (2022) e202103168.

[22] M. Rana, P. Chowdhury, Nonlinear optical responses of organic based indole derivative: an experimental and computational study, Mater. Today. 28 (2020) 241–245.

[23] H.H. Al-Hujaj, Qusay M.A. Hassan, F.A. Almashal, H.A. Sultan, A.M. Dhumad, A. M. Jassem, C.A. Emshary, Benzenesulfonamide-thiazole system bearing an azide group: Synthesis and evaluation of its optical nonlinear responses, Optik 265 (2022) 169477.

[24] M. Khalid, M.U. Khan, I. Shafiq, R. Hussain, K. Mahmood, A. Hussain, R. Jawaria, A. Hussain, M. Imran, M.A. Assiri, NLO potential exploration for D–π–A heterocyclic organic compounds by incorporation of various π-linkers and acceptor units, Arab, J. Chem. 14 (2021) 103295.

[25] M.F. Zaini, W.M. Khairul, S. Arshad, M. Abdullah, D.A. Zainuri, R. Rahamathullah, M.I. Rosli, M.S. Abd Aziz, I.A. Razak, The structure-property studies and mechanism of optical limiting action of methyl 4-((4-aminophenyl) ethynyl) benzoate crystal under continuous wave laser excitation, Opt. Mater. 107 (2020) 110087.

[26] R. Farooq, Z. Batool, M. Khalid, M.U. Khan, A.A.C. Braga, A.H. Ragab, S.R. Al-Mhyawi, G. Muhammad, Z. Shafiq, Synthesis, nonlinear optical analysis and DFT studies of D–π–D and A–π–A configured Schiff bases derived from bis-phenylenediamine, 12, RSC advances., 2022, pp. 32185–32196.

[27] A.U. Hassan, S.H. Sumrra, G. Mustafa, M. Zubair, A. Mohyuddin, S. Noreen, M. Imran, Creating intense and refined NLO responses by utilizing dual donor structural designs in A-π-D-π-D-π-A type organic switches: computed device parameters, Struct. Chem. 34 (2023) 2021–2038.

[28] Y. Cui, J. Cao, J. Lin, C. Li, J. Yao, K. Liu, A. Hou, Z. Guo, J. Zhao, Q. Liu, Advancing nonlinear optics: discovery and characterization of new non-centrosymmetric phenazine-based halides, Dalton. Trans. 53 (2024) 10235–10243.

[29] K.G. von Eschwege, Synthesis and kinetics of electronically altered photochromic dithizonatophenylmercury (II) complexes, J. Photochem. Photobiol. 252 (2013) 159–166.

[30] A.A. Adeniyi, P.-F.X. von Stein, G.W. Bosman, C.M. Steenkamp, T. Chiweshe, K. G. von Eschwege, J. Conradie, Probing ultrafast reaction mechanisms of photo-excited dithizone through transient absorption spectroscopy and computational CASSCF studies, J. Opt. Soc. Am. B 37 (2020) A356–A366.

[31] T. Schönherr, R. Linder, U. Rosellen, V. Schmid, Spectroscopic and quantum chemical study on electronic and geometric properties of free and embedded dithizone molecules, Int. J. Quantum. Chem. 86 (2002) 90–99.

[32] E. Woźnica, M.M. Wójcik, M. Wojciechowski, J.z. Mieczkowski, E. Bulska, K. Maksymiuk, A. Michalska, Dithizone modified gold nanoparticles films for potentiometric sensing, Anal. Chem. 84 (2012) 4437–4442.

[33] G.M. Taha, M.N. Rashed, M.S.A. El-Sadek, M.A.E.-f. Moghazy, Multiferroic BiFeO3 dithizone functionalized as optical sensor for detection and determination of some heavy metals in environmental samples, Bull. Mater. Sci. 44 (2021) 122.

[34] G. Alberti, S. Re, A.M.C. Tivelli, R. Biesuz, Smart sensory materials for divalent cations: A dithizone immobilized membrane for optical analysis, Analyst 141 (2016) 6140–6148.

[35] A. Lukasiewicz, I. Woźniak, P. Fiedor, W. Rowiński, A. Mazurek, I. Licińska, Iodo-derivatives of dithizone with potential diagnostic application, Acta Pol. Pharm. 51 (1994) 513–515.

[36] J.H. Billman, E.S. Cleland, An improved method for the preparation of dithizone (diphenylthiocarbazone), J. Am. Chem. Soc. 65 (1943) 1300–1301.

[37] F. Mirkhalaf, D. Whittaker, D. Schiffrin, Electrochemistry of ITO and gold electrodes covalently modified with dithizone and the effect of Cu (II) and Pb (II) ions, J. Electroanal. Chem. 452 (1998) 203–213.

[38] A.H. Ali, A.M. Jassem, H.A. Sultan, Qusay M.A. Hassan, C.A. Emshary, Thermal and nonlinear optical performances of a new fluid of isatin–oxadiazole hybrid: synthesis and experimental approach, J. Mater. Sci: Mater. Electron. 36 (2025) 1383.

[39] A.H. Ali, H.A. Sultan, Qusay M.A. Hassan, C.A. Emshary, Thermal and nonlinear optical properties of sudan III, J. Fluoresc. 34 (2024) 635–653.

[40] P. Garnuszek, I. Liciñska, P. Fiedor, A.P. Mazurek, The synthesis, radioiodination and preliminary biological study of the new carboxylic derivatives of dithizone, Appl. Radiat. Isot. 49 (1998) 1563–1571.

[41] A.M. Jassem, C.A. Emshary, B.A. Saeed, H.A. Sultan, Q.M.A. Hassan, Visible light-assisted photocatalyst-free synthesis, characterization, theoretical, and nonlinear optical performance of a new 1,3,4-oxadiazole derivative, J. Electron. Mater. 54 (2025) 9939–9959.

[42] R. Dennington, T. Keith, J. Millam, G. View, 5.0, Gaussian, Inc. (2008) 20.

[43] M. Frisch, G. Trucks, H.B. Schlegel, G. Scuseria, M. Robb, J. Cheeseman, G. Scalmani, V. Barone, B. Mennucci, G. Petersson, Gaussian Inc, Wallingford Ct, 2009 (2009).

[44] W.A. Radhi, T.E. Jasim, A.M. Jassem, Exploring of new poly (thiourea-amide) as a prospective Bismarck Brown Y dye adsorbent: synthesis via ultrasound irradiation, isotherms, kinetic, thermodynamic, and DFT studies, J. Indian Chem. Soc. 101 (2024) 101329.

[45] U.J. Al-Hamdani, A.K. Hashim, A.M. Jassem, S.M. Ismael, Effect of mesogenic linkages on two novel aromatic series-based liquid crystals: synthesis, theoretical and comparative studies, Liq. Cryst. 52 (2025) 125–139.

[46] A. Jassem, A. Raheemah, W. Radhi, A. Alid, H. Jaber, Highly diastereoselective metal-free catalytic synthesis of drug-like spiroimidazolidinone, Russ. J. Org. Chem. 55 (2019) 1598–1603.

[47] W. Radhi, T. Jasim, A. Jassem, Adsorptive performance of new poly (Thiourea-Amide) for the efficient removal of Congo red: sonochemical synthesis, isotherm, kinetic, thermodynamic, and DFT studies, Mor. J. Chem. 13 (2025) 325–345.

[48] N. Moorthy, P.J. Prabakar, S. Ramalingam, M. Govindarajan, S.J. Gnanamuthu, G. Pandian, Spectroscopic analysis, AIM, NLO and VCD investigations of acetaldehyde thiosemicarbazone using quantum mechanical simulations, J. Phys. Chem. Solids 95 (2016) 74–88.

[49] X.-H. Li, Z. Mei, X.-Z. Zhang, Computational study of the vibrational spectroscopic studies, natural bond orbital, frontier molecular orbital and second-order non-

linear optical properties of acetophenone thiosemicarbazone molecule, Spectrochim. Acta - A: Mol. Biomol. 118 (2014) 543–551.

[50] S. Bullo, R. Jawaria, I. Faiz, I. Shafiq, M. Khalid, M.A. Asghar, R. Baby, R. Orfali, S. Perveen, Efficient synthesis, spectroscopic characterization, and nonlinear optical properties of novel salicylaldehyde-based thiosemicarbazones: experimental and theoretical studies, ACS Omega 8 (2023) 13982–13992.

[51] S. Muhammad, R.A. Shehzad, J. Iqbal, A.G. Al-Sehemi, M. Saravanabhavan, M. Khalid, Benchmark study of the linear and nonlinear optical polarizabilities in proto-type NLO molecule of para-nitroaniline, J. Theor. Comput. Chem. 18 (2019) 1950030.

[52] R. Jawaria, M. Hussain, M. Khalid, M.U. Khan, M.N. Tahir, M.M. Naseer, A.A. C. Braga, Synthesis, crystal structure analysis, spectral characterization and nonlinear optical exploration of potent thiosemicarbazones based compounds: A DFT refine experimental study, Inorg. Chim. Acta. 486 (2019) 162–171.

[53] M. Adeel, A.A. Braga, M.N. Tahir, F. Haq, M. Khalid, M.A. Halim, Synthesis, X-ray crystallographic, spectroscopic and computational studies of aminothiazole derivatives, J. Mol. Struct. 1131 (2017) 136–148.

[54] C. James, A.A. Raj, R. Reghunathan, V. Jayakumar, I.H. Joe, Structural conformation and vibrational spectroscopic studies of 2, 6-bis (p-N, N-dimethyl benzylidene) cyclohexanone using density functional theory, J. Raman. Spectrosc. 37 (2006) 1381–1392.

[55] M. Khalid, A. Ali, M. Adeel, Z.U. Din, M.N. Tahir, E. Rodrigues-Filho, J. Iqbal, M. U. Khan, Facile preparation, characterization, SC-XRD and DFT/DTDFT study of diversely functionalized unsymmetrical bis-aryl-α, β-unsaturated ketone derivatives, J. Mol. Struct. 1206 (2020) 127755.

[56] A.H. Ali, H. A.Sultan, Qusay M.A. Hassan, C.A. Emshary, Study of the thermal and nonlinear optical properties of alizaringelb R solution, Opt. Quantum Electron. 56 (2024) 1457.

[57] G.P. Agrawal, Modulation instability by cross –phase modulation, Phys. Rev. Lett. 59 (1987) 880–883.

[58] E. Santamato, Y.R. Shen, Field curvature effect on the diffraction ring pattern of laser beam dressed by spatial self-phase modulation in animatic film, Opt. Lett. 9 (1984) 564–566.

[59] L. Deng, He K, T. Zhou, C. Li, Formation and evolution of Far-filed diffraction patterns of divregean and convergant Ganssian beam passing through self-focusing and self-defocusing media, J. Opt. A: Pure Appl. 7 (2005) 409–415.

[60] S. Chavez –Cerda, C.M. Nascimento, M.A.R.C. Alencar, M.G.A. da silva, M.R. Mene ghetto, J.M. Hickman, Experimental observation of the Far field diffraction pattern of divergent and convergent Gaussian beam in a self-defocusing medium, Annals. Opt. XXIX (2006) 1–4.

[61] K. Ogusu, H.Shao Y.Kohtani, Laser- induced diffraction rings from an absorbing solution, Opt. Rev. 3 (1993) 232–234.

[62] R. Santhakumari, K. Ramamurthi, G. Vasuki, B.M. Yamin, G. Bhagavannarayana, Synthesis and spectral characterization of acetophenone thiosemicarbazone—A nonlinear optical material, Spectrochim. Acta - A: Mol. Biomol. 76 (2010) 369–375.

[63] R. Santhakumari, K. Ramamurthi, Structural, thermal and optical characterization of an organic NLO material—Benzaldehyde thiosemicarbazone monohydrate single crystals, Spectrochim. Acta - A: Mol. Biomol. 78 (2011) 653–659.

[64] R. Hanumantharao, S. Kalainathan, G. Bhagavannarayana, Growth, spectral, optical, thermal, crystallization perfection and nonlinear optical studies of novel nonlinear optical crystal—Urea thiosemicarbazone monohydrate, Spectrochim. Acta - A: Mol. Biomol. 91 (2012) 345–351.

[65] A.E. Masunov, A. Tannu, A.A. Dyakov, A.D. Matveeva, A.Y. Freidzon, A. V. Odinokov, A.A. Bagaturyants, First principles crystal engineering of nonlinear optical materials. I. Prototypical case of urea, J. Chem. Phys. (2017) 146.

[66] M.N. Özişik, H.R. Orlande, M.J. Colaço, R.M. Cotta, Finite difference methods in heat transfer, CRC press, 2017.

[67] R. Karimzadeh, Spatial self-phase modulation of a laser beam propagation through liquids with self-induced natural convection flow, J. Opt. 14 (2012) 095701.

[68] R. Karimzadeh, Studies of spatial self-phase modulation of a laser beam passing through liquids, Opt. Commun. 286 (2013) 329–333.